Thin-Walled Structures 171 (2022) 108668

Contents lists available at ScienceDirect

Thin-Walled Structures

journal homepage: www.elsevier.com/locate/tws

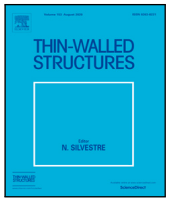

Full length article

Block shear performance of double-line bolted S690 steel angles under uniaxial tension

Ke Ke [a,b], Mingyuan Zhang [c], Michael C.H. Yam [d,e], Angus C.C. Lam [f], Junjie Wang [a,*], Binghui Jiang [g]

[a] School of Civil Engineering, Chongqing University, Chongqing, China
[b] Key Laboratory of New Technology for Construction of Cities in Mountain Area (Chongqing University), Ministry of Education, Chongqing, China
[c] College of Civil Engineering, Hunan University, Changsha, China
[d] Department of Building and Real Estate, Hong Kong Polytechnic University, Hong Kong, China
[e] Chinese National Engineering Research Centre for Steel Construction (Hong Kong Branch), Hong Kong Polytechnic University, Hong Kong, China
[f] Department of Civil & Environmental Engineering, University of Macau, Macau, China
[g] School of Civil Engineering, Central South University, Changsha, China

ARTICLE INFO

Keywords:
Block shear
High-strength steel
Bolted connection
Numerical simulation
Connection capacity

ABSTRACT

We investigated the block shear performance of 16 steel angle specimens connected by double-line bolts. Among these specimens, 10 were made of S690 high-strength steel and 6 were made of normal-strength steel. The angle specimens were fabricated using two hot-rolled steel plates through groove welding. Two angle sections, i.e., 125 × 65 × 6 and 125 × 85 × 6 mm (long leg length × short leg length × thickness), were considered in the test. All angles were connected to the long leg. Apart from steel grade, the test parameters included bolt rows, parallel pitch, transverse pitch, edge distance, and unconnected leg length. Typical block shear of specimens were observed, and different fracture patterns were characterised. The test results confirmed that the block shear strength of the tension angles could be improved by increasing the tension plane area with the increase of the transverse pitch and edge distance and increasing the shear plane area with the increase of the bolt row number and parallel pitch. However, the test results showed that the block shear strength of the angles was not affected by the length of the unconnected leg. Subsequently, numerical models were built to further investigate the block shear behaviour of the double-line bolted angles, and the analysis parameters were the end distance, unconnected leg length, and connected leg length. According to the experimental and numerical results, the accuracy and adequacy of design specifications in the United States, Europe, Canada, and Japan and design equations documented in the literature for evaluating the block shear performance of double-line bolted steel angles were evaluated.

1. Introduction

Bolted connections are frequently used to transfer tension between angles and adjacent structural elements, such as gusset plates. Bolt failure in a bolted tension angle may be effectively suppressed by using high-strength bolts [1]. In this situation, as shown in Fig. 1, block shear failure, characterised by the tearing off of the connecting components, may become the dominant failure mode. The shear yielding or rupture along the shear plane (parallel to the axial load) and tensile fracture along the tension plane (perpendicular to the axial load) are typical characteristics of block shear failure. In practice, for the sake of simplicity, only one leg of an angle is usually connected, which may aggravate the uneven stress distribution over the angle section at the connection region. Consequently, the block shear behaviour may be adversely affected.

In parallel with the block shear behaviour of coped beams [2–6], the research community has explored the block shear strength of tension members [1,7–16]. For example, Orbison et al. [1] investigated the block shear performance of steel angles with single-line bolted connections. Madugula and Mohan [9] reviewed the test data pool of steel tension angles dominated by block shear failure and summarised the influential parameters. Epstein [10] experimentally investigated the block shear performance of tension angles by considering different connection configurations. Cunninghan et al. [11] and Kulak and Grondin [12] evaluated the accuracy of design codes worldwide, and it was confirmed that the existing specifications had drawbacks in predicting the block shear strength or failure modes. Subsequently, refined design approaches have also been developed. Using a finite element data pool, Topkaya [13] established a practical approach for

* Corresponding author.
E-mail address: ruida91@outlook.com (J. Wang).

https://doi.org/10.1016/j.tws.2021.108668
Received 21 June 2021; Received in revised form 11 October 2021; Accepted 7 November 2021
Available online 13 December 2021

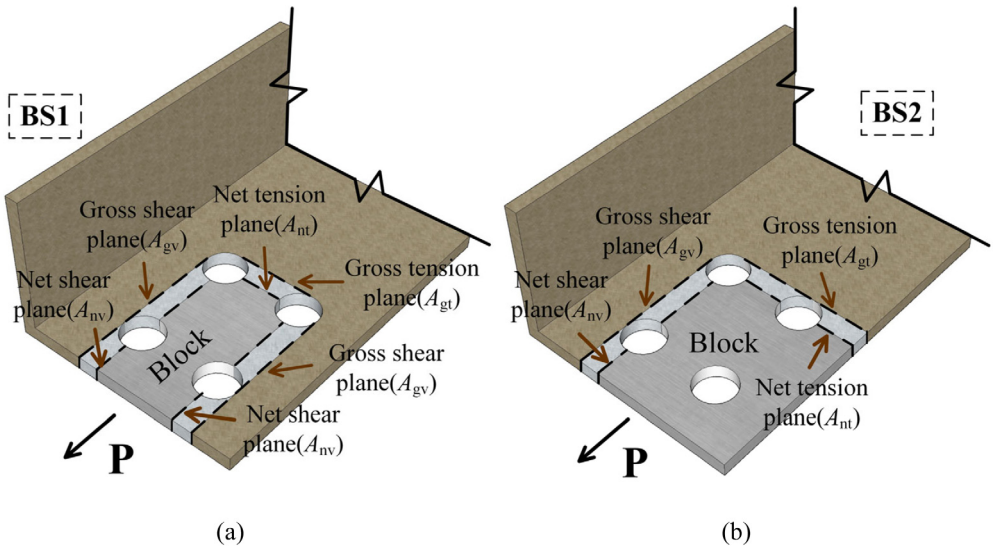

Fig. 1. Block shear failure of a bolted steel angle: (a) BS1 mode and (b) BS2 mode.

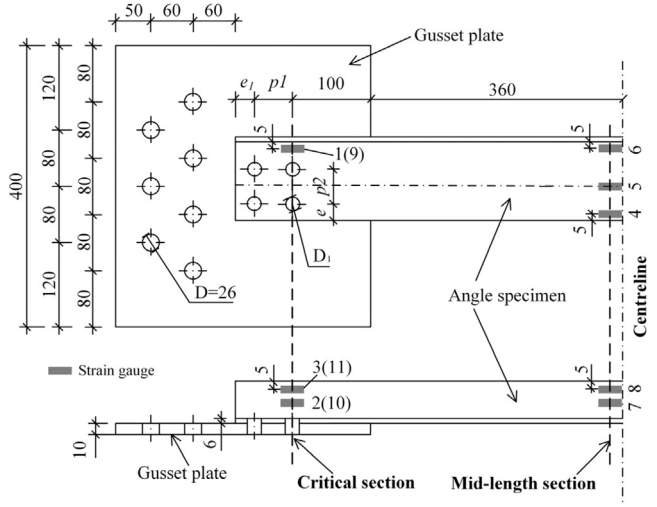

Fig. 2. Typical test specimen.

designing tension members governed by block shear. Samimi et al. [16] explored the block shear performance of steel channels connected by staggered bolts. All the aforementioned studies focused on block shear behaviour of normal strength steel (NSS) tension members with a yield strength of <460 MPa.

Compared to NSS, the use of high strength steel (HSS) with a yield strength of ≥460 MPa [17] can reduce the weight and size of structures and foundations, saving material and construction costs. Therefore, the advantage of HSS-based construction has promoted advances in research on HSS material behaviour [17–21], mechanical behaviour of HSS connections/components [22–30], and HSS structural systems [31–35]. Nevertheless, the lower ductility of HSS than that of NSS, which was characterised in previous studies [17,18,23], is a major limitation of the material. In tension members that fail because of block shear failure, the poorer ductility of HSS may compromise the stress redistribution ability at the critical section of the shear block, exposing the members to a higher risk of premature fracture.

In recent decades, the research community has examined the block shear behaviour of bolted tension members made of HSS. Gross et al. [36] studied the block shear performance of HSS tension angles and re-examined the adequacy of the design codes for computing the block shear strength of the angles. Teh's research group [37,38] proposed design equations for predicting the block shear strength of cold-formed HSS connections, and were able to achieve an enhanced accuracy over that of the methods described in design specifications [39–42]. Teh and Deierlein [43] later established a modified approach for quantifying the block shear strength of hot-formed steel members, and the feasibility of the method was confirmed using the available test data in literature. More recently, based on a full-scale test programme, Jiang et al. [44] evaluated the adequacy of the design equations in the above-mentioned literature and design codes for predicting the block shear strength of S690 HSS angles connected by single-line bolts. Although these studies provide useful information on the block shear performance of bolted HSS tension angles, the focus of these studies was on steel plates or single-line bolted angles, whereas the load-carrying mechanism of HSS tension angles with double-line bolted connections remains unclear, and more experimental data and numerical analyses are needed.

The primary research objectives of the current study are twofold: (i) to provide experimental data for designing the block shear strength of double-line bolted S690 HSS tension angles and (ii) to investigate the effect of the relatively low ductility of S690 HSS on the performance of double-line bolted tension angles. The test parameters include steel grade, bolt row number, parallel pitch, transverse pitch, edge distance, and unconnected leg length. Subsequently, using calibrated finite element (FE) models, detailed numerical analyses of angle sections and connection configurations within a reasonable range were performed to study their effects on the block shear performance. By comparing the experimental and numerical results, the applicability of the design equations in the aforementioned literature and design codes for computing the block shear strength of double-line bolted S690 HSS angles was examined.

2. Current design equations for block shear capacity

The design equations for block shear capacity that have been documented in the major design specifications and prior literature are listed in Table 1. Accordingly, the block shear strength includes two parts: (i) the tensile resistance of the tension plane and (ii) the shear resistance of the shear plane. Note that the calculation methods for the tensile and shear resistances are different for different equations, as different assumptions are made.

For the contribution of the tension plane, in all design equations, except for those of CSA [41] and Teh and Yazici [38], it is assumed that the tension plane fails because of tensile rupture; hence, the tensile resistance of the tension plane was determined by the ultimate tensile

Table 1
Design equations for block shear capacity.

Design specifications	Design equations	Assumptions
AISC [39]	$P_{AISC} = U_{bs} f_u A_{nt} + 0.60 f_u A_{nv} \le U_{bs} f_u A_{nt} + 0.60 f_y A_{gv}$	"net tension plane fracture" + "'net shear plane fracture' or 'gross shear plane yielding'" + "Mises criterion"
Eurocode 3 [40]	$P_{EC3} = f_u A_{nt} + (1/\sqrt{3})\ f_y A_{nv}$	"net tension plane fracture" + "net shear plane yielding" + "Mises criterion"
CSA [41]	$P_{CSA} = U_t f_u A_{nt} + 0.60\ A_{gv}(f_y + f_u)/2$, ($f_y \le 460$ MPa) $P_{CSA} = U_t f_u A_{nt} + 0.60\ A_{gv} f_y$, ($f_y > 460$ MPa)	"net tension plane fracture" + "gross shear plane yielding" + "Mises criterion"
AIJ [42]	$P_{AIJ} = f_u A_{nt} + 0.5 f_y A_{gv}$	"net tension plane fracture" + "gross shear plane yielding" + "Tresca criterion"
Topkaya [13]	$P_{Top} = f_u A_{nt} + (0.2 + 0.35 f_u/f_y)\ f_y A_{gv}$	"net tension plane fracture" + "gross shear plane yielding"
Teh and Yazici [38]	$P_{T\&Y} = (0.9 + 0.05\ d/e)\ f_u A_{nt} + 0.6 f_y A_{av}$	"net tension plane fracture" + "active shear plane yielding" + "Mises criterion"
Teh and Deierlein [43]	$P_{T\&D} = f_u A_{nt} + 0.6 f_u A_{av}$	"net tension plane fracture" + "active shear plane fracture" + "Mises criterion"

Notes: U_{bs} = 1.0 for tension angles with bolted connection; U_t = 0.6 for angles connected by one leg; f_y = yield stress, f_u = tensile strength, A_{nt} = net tension area, A_{nv} = net shear area, A_{gv} = gross shear area, d = bolt shank diameter, e = edge distance, A_{av} = active shear plane = $(A_{gv}+A_{nv})/2$.

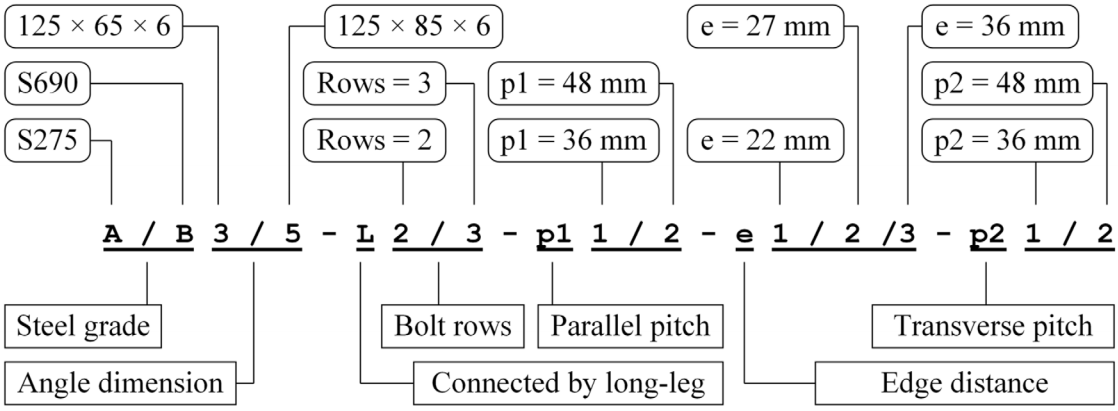

Fig. 3. Nomenclature of the test specimen.

resistance. Comparatively, the detrimental effect of uneven stress distribution over the tension plane has been accounted for in CSA [41] and in the study by Teh and Yazici [38], in which reduction factors were employed.

The difference in shear resistance in these design equations is caused by the different assumptions made for the shear failure plane and material failure criteria. In CSA [41], AIJ [42], and Topkaya [13], shear failure was mainly determined by the yield of the gross shear plane. In contrast, in Eurocode 3 [40], the shear plane is assumed to fail because of the yielding of the net shear plane. In AISC [39], shear failure is presumed to be governed by the yield of the gross shear plane or shear fracture of the net shear plane. Teh and Yazici [38] assumed that shear resistance is dominated by the yield of an active shear plane located between the net and gross shear planes, while Teh and Deierlein [43] presumed that shear resistance is governed by the fracture of the active shear plane. Notably, apart from AIJ [42], in which the Tresca criterion for quantifying the failure criterion was used, AISC [39], Eurocode 3 [40], CSA [41], Teh and Yazici [38], and Teh and Deierlein [43] adopted the von Mises criterion. In particular, the shear yield strength of the material governed by the Tresca criterion is equal to half of the tensile strength. For the von Mises criterion, this ratio was approximately equal to 0.6. In contrast, the design equation proposed by Topkaya [13] uses neither of the two criteria, as the shear yield strength is a nominal quantity determined by a regression analysis based on a numerical database. CSA [41] considered the contribution of strain hardening when determining the strength of the shear plane in the case of NSS material, whereas post-yielding strain hardening is ignored for HSS materials with a yield strength of >460 MPa.

3. Experimental programme

Sixteen tension angle specimens connected by double-line bolts were designed and tested to investigate their block shear performance. The main test variables included (i) steel grade, (ii) row number of

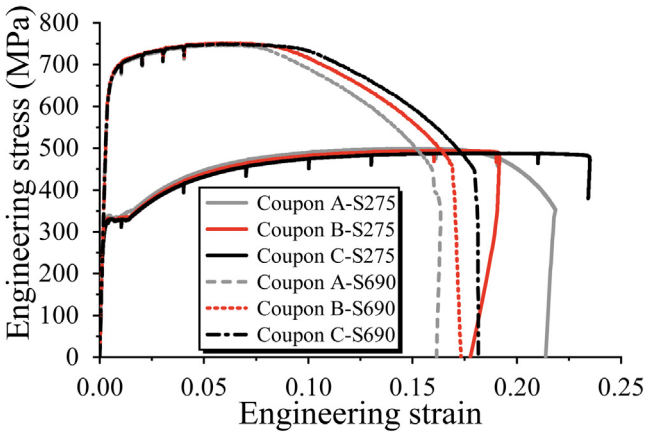

Fig. 4. Coupon test results.

double-line bolts, (iii) parallel pitch (p1), (iv) transverse pitch (p2), (v) edge distance (e), and (vi) length of the legs. The symbols of the parameters are also indicated in a typical test specimen, as shown in Fig. 2. The nomenclature for each specimen is shown in Fig. 3. Table 2 lists the details and measured dimensions of all the specimens. Ten specimens (B series) were made of S690 HSS, and six specimens (A series) were made of S275 NSS. The angle specimens were fabricated using two hot-rolled steel plates through groove welding. Two angle sections, that is, 125 × 65 × 6 and 125 × 85 × 6 mm (long leg length × short leg length × thickness), were considered in the parameter matrix. All angles were connected to the long leg. The number of bolt rows considered was two and three. Two pitch values of 36 and 48 mm were designed for both parallel and transverse pitches, respectively. The three designed edge distances were 22, 27, and 36 mm. The material

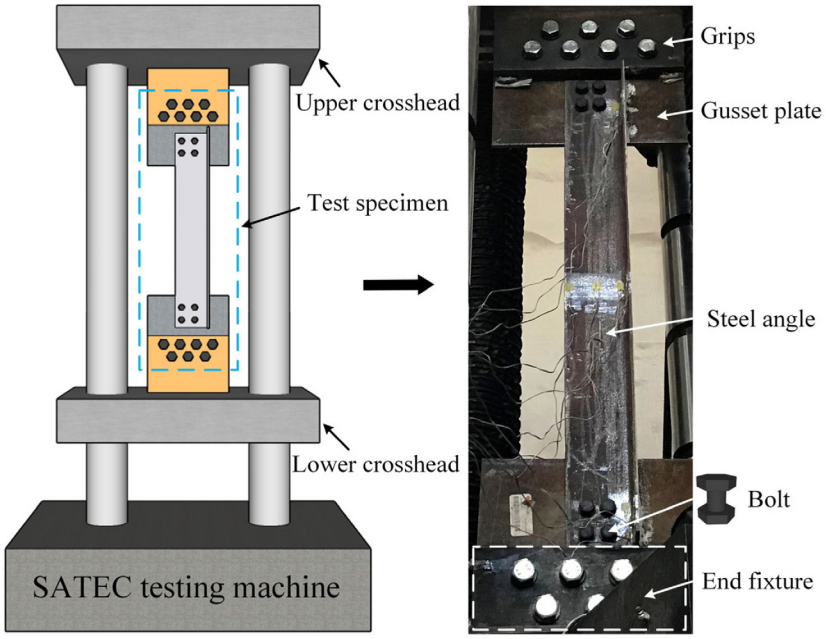

Fig. 5. Test arrangement.

Table 2
Summary of test specimens and results.

Specimen	Dimension (mm)	Steel grade	Bolt rows	p1 (mm)	p2 (mm)	e (mm)	Failure mode	Aspect ratio	P_{test} (kN)	P_{FE} (kN)	P_{test}/P_{FE}	Error (%)
B3-L2-p12-e1-p22	125 × 65 × 6	S690	2	47.7	47.4	22.6	BS2	1.035	340.25	344.98	0.99	1.37%
B3-L2-p12-e2-p22	125 × 65 × 6	S690	2	47.9	47.5	27.4	BS2	0.973	372.79	368.50	1.01	−1.16%
B3-L2-p12-e3-p22	125 × 65 × 6	S690	2	46.7	48.7	34.8	BS2	0.863	398.55	403.51	0.99	1.23%
B3-L2-p12-e3-p21	125 × 65 × 6	S690	2	48.6	35.7	36.2	BS2	1.023	343.85	353.09	0.97	2.62%
B3-L2-p11-e3-p22	125 × 65 × 6	S690	2	34.9	48.1	34.8	BS1	0.722	362.78	371.44	0.98	2.33%
B3-L3-p12-e3-p22	125 × 65 × 6	S690	3	48.1	48.6	35.8	BS2	1.428	485.53	479.07	1.01	−1.35%
B3-L3-p12-e3-p21	125 × 65 × 6	S690	3	47.5	35.8	35.9	BS2	1.658	428.95	419.07	1.02	−2.36%
B3-L3-p11-e3-p22	125 × 65 × 6	S690	3	36.5	49.1	35.8	BS2	1.153	434.75	447.16	0.97	2.78%
B5-L2-p12-e1-p22	125 × 85 × 6	S690	2	47.9	48.3	21.7	BS2	1.038	332.01	340.49	0.98	2.49%
B5-L2-p12-e3-p22	125 × 85 × 6	S690	2	47.8	48.2	35.3	BS2	0.873	402.82	404.86	0.99	0.50%
										Mean	0.99	
										CoV	0.018	
A3-L2-p12-e1-p22	125 × 65 × 6	S275	2	47.6	47.5	22.6	BS2	1.033	217.43	220.62	0.99	1.44%
A3-L2-p12-e3-p22	125 × 65 × 6	S275	2	48.1	47.9	36.4	BS2	0.859	259.13	261.90	0.99	1.06%
A3-L2-p12-e3-p21	125 × 65 × 6	S275	2	47.6	36.0	36.1	BS2	0.997	223.48	220.86	1.01	−1.18%
A3-L2-p11-e3-p22	125 × 65 × 6	S275	2	35.8	47.8	35.7	BS1	0.724	233.67	242.20	0.96	3.52%
A3-L3-p12-e3-p21	125 × 65 × 6	S275	3	47.4	36.0	35.9	BS2	1.644	243.01	267.39	0.91	9.12%
A3-L3-p11-e3-p22	125 × 65 × 6	S275	3	35.6	48.1	36.2	BS2	1.125	284.46	287.14	0.99	0.93%
										Mean	0.98	
										CoV	0.034	

Table 3
Summary of material properties.

Material	Elastic modulus (GPa)	Yield stress f_y (MPa)	Tensile strength f_u (MPa)	Ultimate strain ε_u	f_u/f_y
S690 angle plate	185	640	715	0.061	1.12
S690 gusset plate	195	705	730	0.060	1.04
S275 angle plate	195	310	470	0.163	1.52

characteristics of the steel angles were obtained through a coupon test following ASTM 370 [45]. As shown in Fig. 4, three coupon tests were conducted for both S275 and S690 steel angles, and the corresponding average values are listed in Table 3. Fig. 4 plots the engineering stress (σ_{eng}) with respect to engineering strain (ε_{eng}) curves for these coupon specimens. As indicated by ε_u in Table 3, the ductility of S690 steel is much lower than that of S275 steel. The steel coupons were extracted from the steel plates that were used to fabricate the steel angles.

Fig. 5 shows the test setup. Both ends of the angle specimens were connected to 10-mm-thick gusset plates using M16 grade 12.9 high-strength bolts (Fig. 2). The gusset plates were fixed to a SATEC testing machine with M24 Grade 12.9 high-strength bolts. The test setup was designed to deform specimens within the elastic range during the test. The displacements of the test specimens and the applied load were recorded using the built-in transducers of the testing machine. As shown in Fig. 2, the longitudinal strains at the mid-length and critical sections were measured using strain gauges. All the bolts were snug-tightened. Before the test, to eliminate the possible slip caused by the gap between the bolt holes and bolt shanks, all the specimens were tightened by applying a small amount of axial load. The loading rate during the test was 0.2 mm/min. The test was terminated upon fracture or significant deterioration of strength. To capture the first

Fig. 6. Failure modes of specimens.

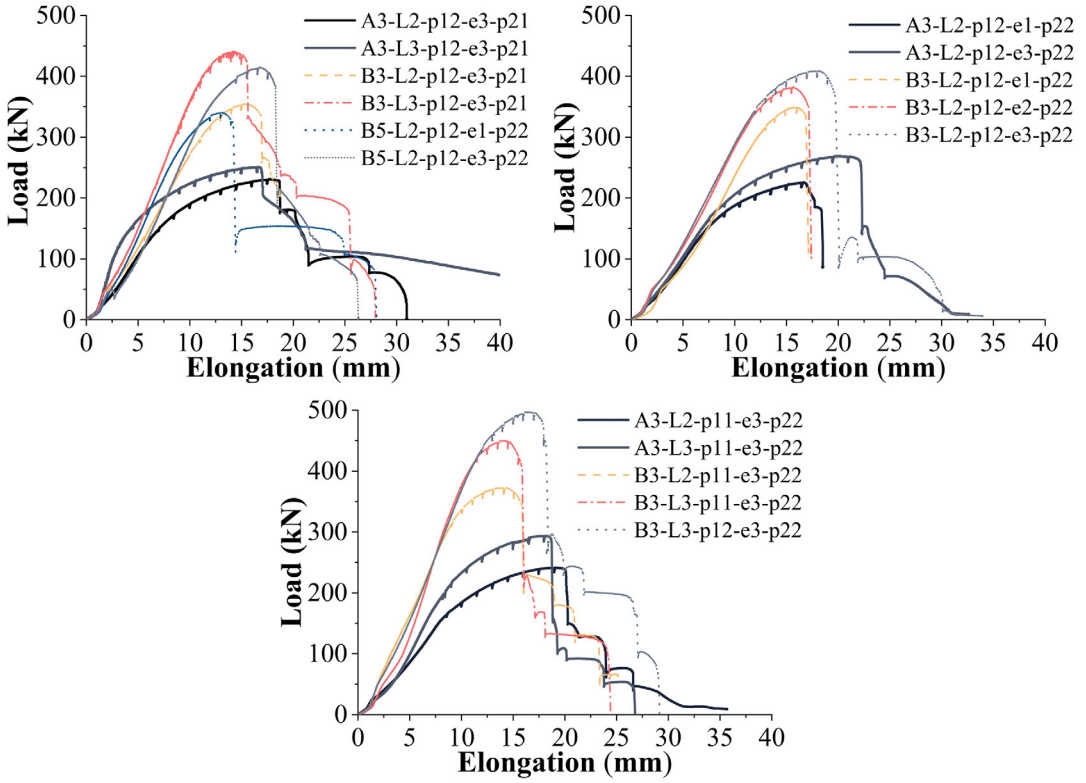

Fig. 7. Load–displacement curves of specimens.

Table 4
Test results summary and comparison.

Variables	Contrastive pairs	Specimens	Ultimate capacity	Ultimate deformation	Specimens	Ultimate capacity	Ultimate deformation	Comparison	Comparison
Steel grade	Pairs	S275	P_{S275} (kN)	Δ_{S275} (mm)	S690	P_{S690} (kN)	Δ_{S690} (mm)	P_{S690}/P_{S275}	$\Delta_{S690}/\Delta_{S275}$
	1	A3-L2-p12-e1-p22	217.43	16.7	B3-L2-p12-e1-p22	340.25	15.7	1.565	0.940
	2	A3-L2-p12-e3-p22	259.13	20.1	B3-L2-p12-e3-p22	398.55	18.2	1.538	0.905
	3	A3-L2-p12-e3-p21	223.48	17.7	B3-L2-p12-e3-p21	343.85	15.2	1.539	0.859
	4	A3-L2-p11-e3-p22	233.67	19.2	B3-L2-p11-e3-p22	362.78	14.3	1.553	0.745
	5	A3-L3-p12-e3-p21	243.01	16.6	B3-L3-p12-e3-p21	428.95	14.2	1.765	0.855
	6	A3-L3-p11-e3-p22	284.46	18.2	B3-L3-p11-e3-p22	434.75	14.1	1.528	0.775
Bolt rows	Pairs	2 bolt rows	P_{2rows} (kN)	Δ_{2rows} (mm)	3 bolt rows	P_{3rows} (kN)	Δ_{3rows} (mm)	P_{3rows}/P_{2rows}	$\Delta_{3rows}/\Delta_{2rows}$
	1	A3-L2-p12-e3-p21	223.48	17.7	A3-L3-p12-e3-p21	243.01	16.6	1.087	0.938
	2	A3-L2-p11-e3-p22	233.67	19.2	A3-L3-p11-e3-p22	284.46	18.2	1.217	0.948
	3	B3-L2-p12-e3-p22	398.55	18.2	B3-L3-p12-e3-p22	485.53	16.3	1.218	0.896
	4	B3-L2-p12-e3-p21	343.85	15.2	B3-L3-p12-e3-p21	428.95	14.2	1.247	0.934
	5	B3-L2-p11-e3-p22	362.78	14.3	B3-L3-p11-e3-p22	434.75	14.1	1.198	0.986
Parallel pitch (p1)	Pairs	p1 = 36 mm	$P_{p1\ =\ 36\ mm}$ (kN)	$\Delta_{p1\ =\ 36\ mm}$ (mm)	p1 = 48 mm	$P_{p1\ =\ 48\ mm}$ (kN)	$\Delta_{p1\ =\ 48\ mm}$ (mm)	$P_{p1\ =\ 48\ mm}/P_{p1\ =\ 36\ mm}$	$\Delta_{p1\ =\ 48\ mm}/\Delta_{p1\ =\ 36\ mm}$
	1	A3-L2-p11-e3-p22	233.67	19.2	A3-L2-p12-e3-p22	259.13	20.1	1.109	1.047
	2	B3-L2-p11-e3-p22	362.78	14.3	B3-L2-p12-e3-p22	398.55	18.2	1.099	1.273
	3	B3-L3-p11-e3-p22	434.75	14.1	B3-L3-p12-e3-p22	485.53	16.3	1.117	1.156
Transverse pitch (p2)	Pairs	p2 = 36 mm	$P_{p2\ =\ 36\ mm}$ (kN)	$\Delta_{p2\ =\ 36\ mm}$ (mm)	p2 = 48 mm	$P_{p2\ =\ 48\ mm}$ (kN)	$\Delta_{p2\ =\ 48\ mm}$ (mm)	$P_{p2\ =\ 48\ mm}/P_{p2\ =\ 36\ mm}$	$\Delta_{p2\ =\ 48\ mm}/\Delta_{p2\ =\ 36\ mm}$
	1	A3-L2-p12-e3-p21	223.48	17.7	A3-L2-p12-e3-p22	259.13	20.1	1.160	1.136
	2	B3-L2-p12-e3-p21	343.85	15.2	B3-L2-p12-e3-p22	398.55	18.2	1.159	1.197
	3	B3-L3-p12-e3-p21	428.95	14.2	B3-L3-p12-e3-p22	485.53	16.3	1.132	1.148
Edge distance (e)	Pairs	e1 = 22 mm	P_{e1} (kN)	Δ_{e1} (mm)	e3 = 36 mm	P_{e3} (kN)	Δ_{e3} (mm)	P_{e3}/P_{e1}	Δ_{e3}/Δ_{e1}
	1	A3-L2-p12-e1-p22	217.43	16.7	A3-L2-p12-e3-p22	259.13	20.1	1.192	1.204
	2	B3-L2-p12-e1-p22	340.25	15.7	B3-L2-p12-e3-p22	398.55	18.2	1.171	1.159
	3	B5-L2-p12-e1-p22	332.01	13.1	B5-L2-p12-e3-p22	402.82	16.7	1.213	1.275
Leg length	Pairs	125 × 65 × 6	P_3 (kN)	Δ_3 (mm)	125 × 85 × 6	P_5 (kN)	Δ_5 (mm)	P_5/P_3	Δ_5/Δ_3
	1	B3-L2-p12-e1-p22	340.25	15.7	B5-L2-p12-e1-p22	332.01	13.1	0.976	0.834
	2	B3-L2-p12-e3-p22	398.55	18.2	B5-L2-p12-e3-p22	402.82	16.7	1.011	0.918

fracture location of the specimens dominated by block shear, tests for specimens B3-L2-p12-e1-p22, B3-L2-p12-e2-p22, B3-L2-p12-e3-p21, A3-L2-p12-e1-p22, and A3-L3-p12-e3-p21 were terminated after the first significant load drop was observed.

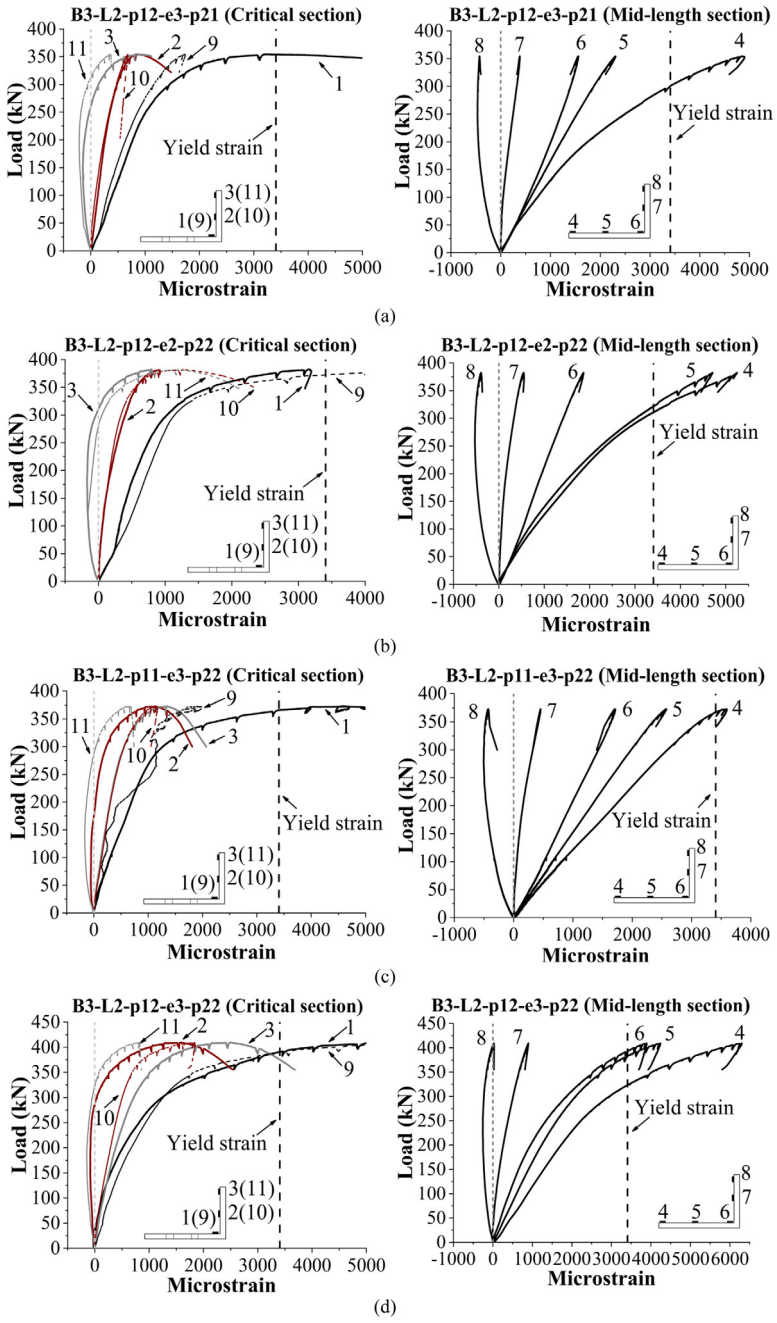

Fig. 8. Axial strain evolution at the critical and mid-length sections: (a) B3-L2-p12-e3-p21, (b) B3-L2-p12-e2-p22, (c) B3-L2-p11-e3-p22, (d) B3-L2-p12-e3-p22, (e) B3-L3-p12-e3-p22, (f) B5-L2-p12-e3-p22, (g) A3-L2-p12-e3-p21, (h) A3-L2-p11-e3-p22 and (i) A3-L2-p12-e3-p22.

4. Experimental results

4.1. Failure modes

Fig. 6 shows photographs of each specimen after testing. According to Fig. 6, the failure of the test specimens is categorised into two failure modes, as shown in Fig. 1. For mode BS1, two shear planes were formed, whereas mode BS2 had only one plane. As shown in Fig. 6 and listed in Table 2, apart from specimens B3-L2-p11-e3-p22 and A3-L2-p11-e3-p22, all specimens were failed by BS2 failure mode as typical block shear failure. As for BS1 failure mode, although evident end tear-out [43] was observed after the termination of the test, as shown in Fig. 6, the two specimens still showed the characteristics of block shear from the perspective of the ultimate strength, including tensile rupture of the tensile plane and shear yielding of the shear plane when the ultimate strength was achieved. This proposition may be further supported by finite element analysis results in later sections. It is also noted that B3-L2-p11-e3-p22 and A3-L2-p11-e3-p22 had the lowest nominal aspect ratio of the block, which is defined by the ratio of the gross shear plane area to the tension plane area. A more detailed discussion regarding this issue is presented in the following sections.

4.2. Load versus elongation response curves

Fig. 7 shows the applied load versus elongation curves of all the specimens. As anticipated, the range of the linear elastic stage of the S690 steel angles is wider than that of the S275 steel angles with the same connection configurations. Owing to the evident difference in strength and negligible discrepancy in the elastic modulus, the elastic stiffness of the S690 steel angles generally matched that of

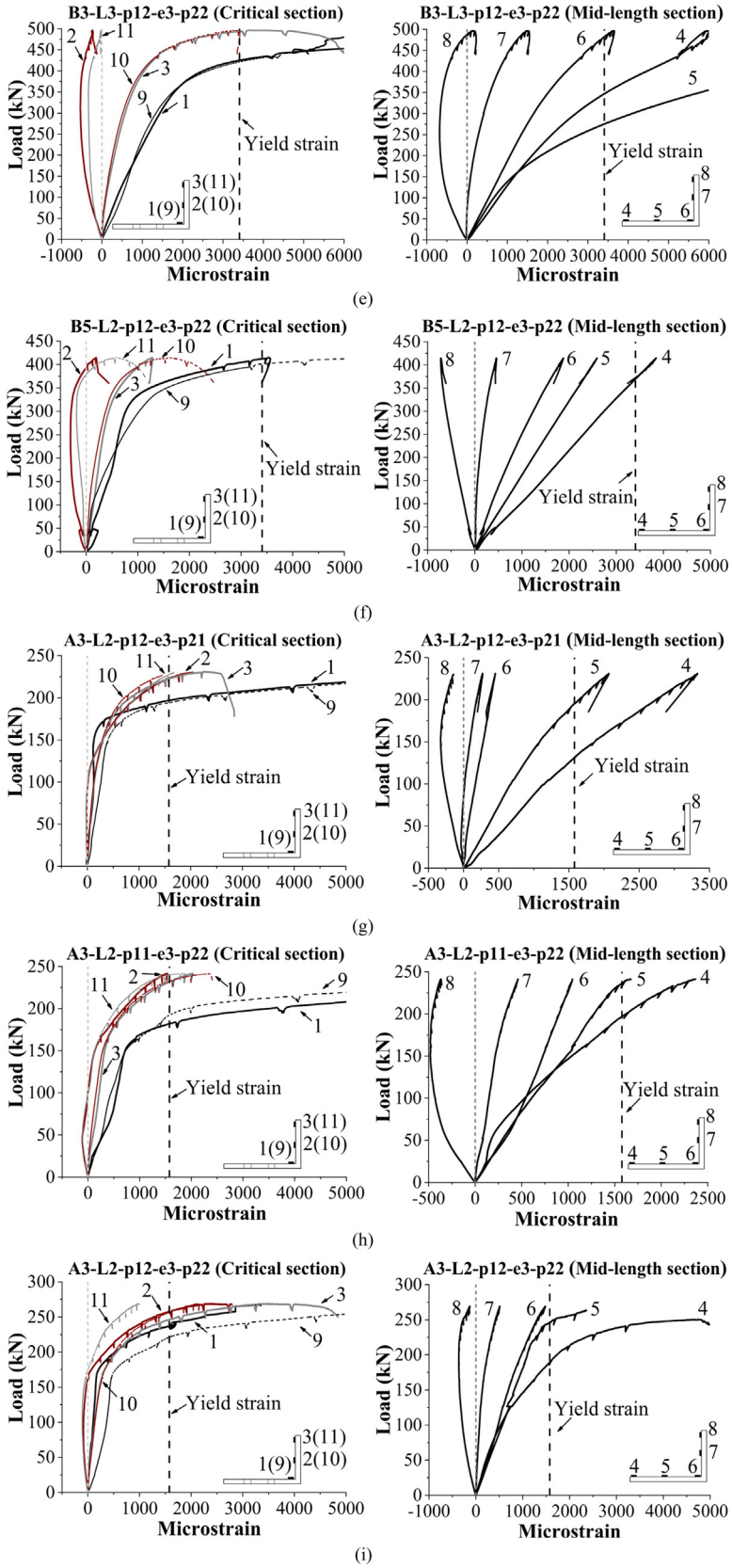

Fig. 8. (*continued*).

the S275 steel angle specimens, whereas yielding of S275 steel angles was triggered at lower deformation levels. The response curves of the S275 steel angles exhibited a wider inelastic deformation spectrum compared to those of the S690 steel angles. Once the ultimate strength was reached, the applied load suddenly dropped due to the cracking of the tension plane. With further displacement, a plateau in the applied

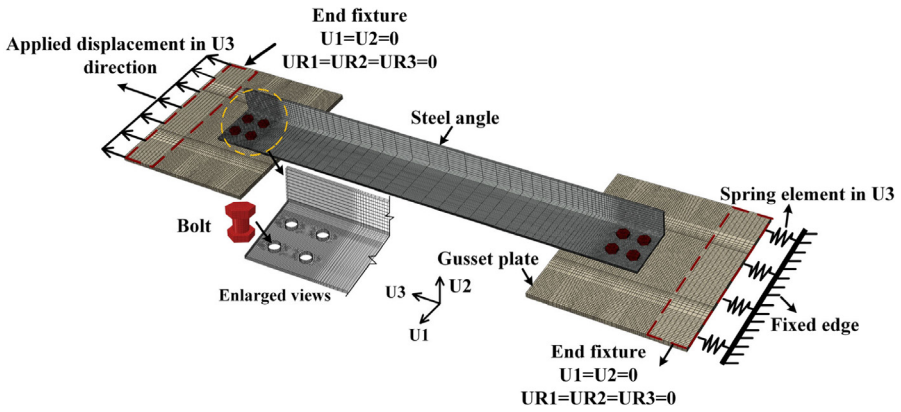

Fig. 9. Overview of finite element model.

load was formed for test specimens with a comparatively larger aspect ratio of the shear block (e.g., B3-L3-p12-e3-p21 and B5-L2-p12-e1-p22), except for cases where the test was terminated. Several specimens exhibited a plateau with a slight increase in strength in the post-ultimate stage. This observation is understandable because sufficient shear yielding was achieved, which is in line with the observations by Teh and Uz [46]. The comparison of specimen pairs with various aspect ratios (e.g., A3-L2-p12-e3-p21/A3-L2-p12-e3-p22 and B5-L2-p12-e1-p22/B5-L2-p12-e3-p22) showed that the plateau of specimens with smaller aspect ratios (e.g., A3-L2-p12-e3-p22 and B5-L2-p12-e3-p22) was not pronounced as strength deterioration was rapid. This may be because a small aspect ratio of the block generally corresponds to a low ratio of the contribution of the shear plane in block shear failure, and fracture of the shear plane is triggered rapidly after the inception of cracking of the tension plane. Notably, the characteristics of the response curves were consistent with the findings by Gross et al. [36] and Jiang et al. [44]. Specifically, according to the load–elongation curves (Fig. 7), the elongation corresponding to the fracture point of the S690 steel specimen is close to that of the S275 steel angles. This observation is interesting because of the discrepancy in material ductility between S275 and S690, as tabulated in Table 3. This could be due to the elastic deformation capacity of the S690 steel angle compensating for the total elongation ability of the specimen.

4.3. Strain responses

Fig. 8 presents the axial strain evolution at the critical and mid-length sections of the selected test specimens. In particular, the strain responses of S690 steel angles (specimens B3-L2-p12-e3-p21, B3-L2-p12-e2-p22, B3-L2-p11-e3-p22, B3-L2-p12-e3-p22, B3-L3-p12-e3-p22, and B5-L2-p12-e3-p22) and S275 steel angles (A3-L2-p12-e3-p21, A3-L2-p11-e3-p22, and A3-L2-p12-e3-p22) are shown in Fig. 8, and the yield strain of each specimen is depicted by the vertical dashed lines. At the critical and mid-length sections, the strain distributions of all specimens were uneven owing to the secondary bending moment and shear lag.

For the critical sections of all test specimens, the tensile strains primarily developed at the connected leg at the initial loading stage. Specifically, the tensile strains of the materials close to the bolt holes (strain gauges 1 and 9) of critical sections developed quickly and exceeded the yield threshold with increasing applied load. For the unconnected leg, owing to the eccentric bending, compressive strains were first observed at the outer end (strain gauges 3 and 11). However, as the applied load increased, the compressive strain decreased and gradually reversed to tensile strain. For the mid-length section, the compressive strain at the unconnected leg was slightly more severe than that of the critical section during the early loading phases owing to the eccentric bending, and this compressive strain was not transformed into tensile strain until the test termination for most of the specimens, except for specimen B3-L3-p12-e3-p22, in which the compression at the toe of the unconnected leg was finally reversed to tension.

For the sake of brevity, the selected comparison pairs summarised in Table 4 were adopted in this study to interpret the strain distributions. By comparing the specimen pairs in the steel grade groups (e.g., B3-L2-p12-e3-p21 and A3-L2-p12-e3-p21), it can be seen that the strain distributions of the S690 and S275 steel angles were similar, confirming the findings of a previous study [44]. For the bolt rows groups (B3-L2-p12-e3-p22 and B3-L3-p12-e3-p22), it can be seen that higher tensile strains and more notable compressive-to-tensile strain evolution trends were observed at the mid-length sections in cases with more bolts. With respect to the influence of parallel pitch, transverse pitch, and edge distance groups, it was also found that compression at the toe of the unconnected leg was alleviated at the mid-length section for specimens with an increasing parallel pitch, transverse pitch, and edge distance. For the leg length group, the unconnected leg length has an obvious effect on the strain distribution mode at the mid-length section. Comparison of the strains at the mid-length sections of specimens B3-L2-p12-e3-p22 and B5-L2-p12-e3-p22 reveals that the compressive strain at the toe of the unconnected leg of specimen B5-L2-p12-e3-p22 with the 125 × 85 × 6 angle section kept increasing until test termination, which was the result of the increased eccentric bending caused by an increasing unconnected leg length.

4.4. Discussion of the test data

According to Fig. 7 and the comparison pairs in Table 4, the strengths of the S690 steel angles were all higher than those of the S275 steel counterparts, as expected. However, owing to the relatively lower ductility of S690 steel, the inelastic deformation range of the B series specimens and the displacements at the ultimate load (Table 4) were all lower than their A series specimen counterparts. This difference was caused by the different mechanical behaviours of the material. In particular, higher values of ε_u and f_u/f_y of S275 steel compared with those of S690 steel facilitated the redistribution of the stress in the vicinity of the block after yielding was triggered. Note that this behaviour is in line with the recent work on single-line S690 steel angles dominated by block shear [44].

In addition, altering the bolt row number and parallel pitch could alter the size of the shear plane, which further affects the contribution of the shear resistance of the block. According to Table 4, the ultimate capacities (P_{2rows} and P_{3rows} in Table 4) and ultimate deformations (Δ_{2rows} and Δ_{3rows}) of the comparison pairs can shed light on the influence of the bolt row number. In particular, after increasing the bolt rows from two to three, the ultimate capacity was significantly enhanced. Nevertheless, the ultimate deformations of the specimens with three bolts were lower than those of the specimens with two bolts.

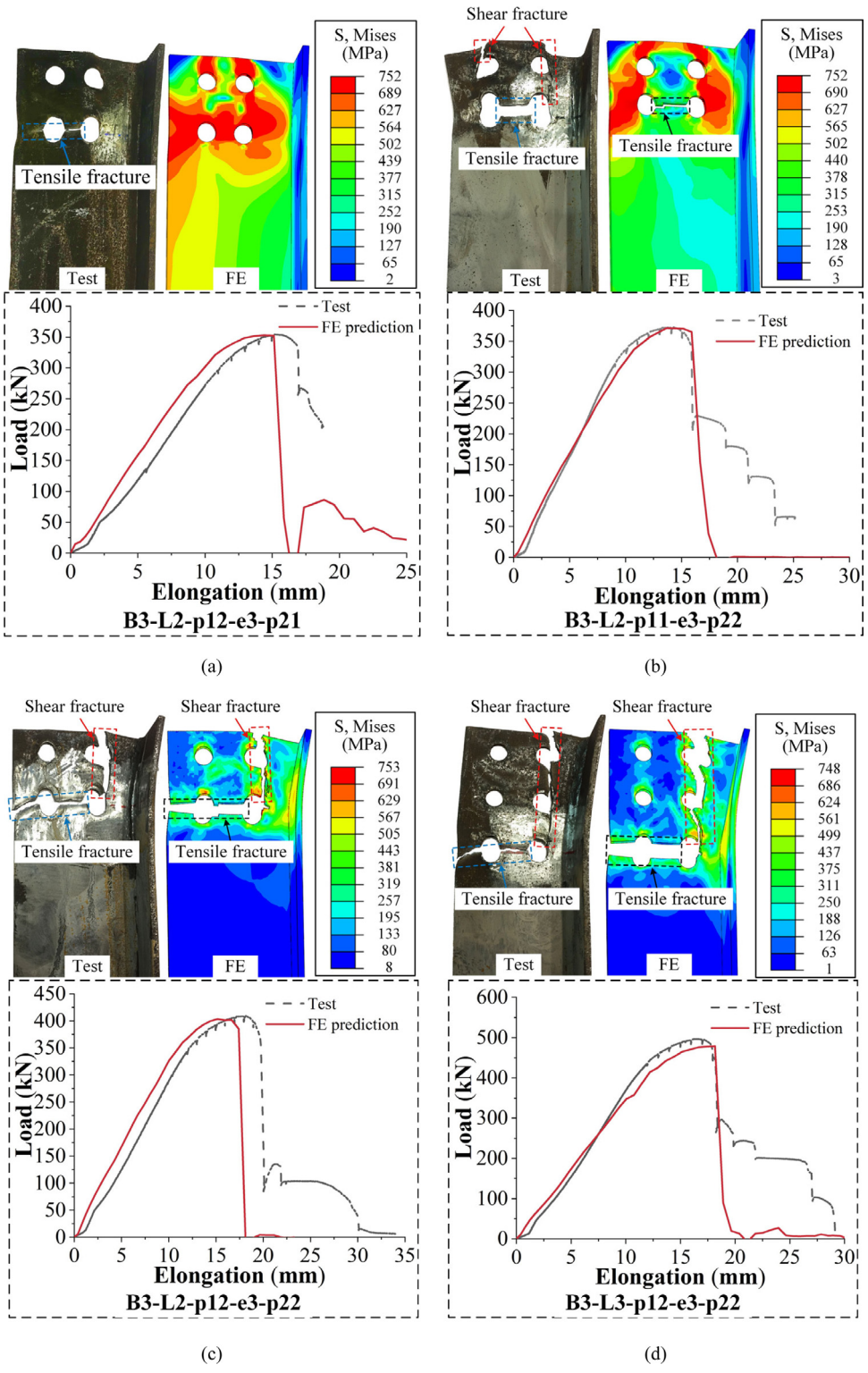

Fig. 10. Comparisons between numerical predictions and test results: (a) B3-L2-p12-e3-p21, (b) B3-L2-p11-e3-p22, (c) B3-L2-p12-e3-p22, (d) B3-L3-p12-e3-p22, (e) B5-L2-p12-e3-p22, (f) A3-L2-p12-e3-p21, (g) A3-L2-p11-e3-p22 and (h) A3-L2-p12-e3-p22.

Table 4 also presents the ultimate capacity and relative comparison of the specimens with varied parallel pitches. As can be seen, with the increase in parallel pitch from 36 to 48 mm, the ultimate capacity increased by at least 9.9%. In addition, the deformation capacity of the specimens was also enhanced after increasing the parallel pitch, as given in Table 4.

In addition, the influence of the transverse pitch and edge distance on the tension plane area can also be observed. It can be confirmed that increasing the transverse pitch from 36 to 48 mm could improve the connection resistance by ≥13.2%, as given in Table 4. In addition, the deformation capacity of the tension angles also increased with increasing transverse pitch. In addition, such influence was not appreciably affected by steel grade, as demonstrated by comparison pairs 1 and 2 in Table 4.

As given in Table 4, an increasing edge distance (i.e., varying from 22 to 36 mm) significantly contributed to the enhanced block shear

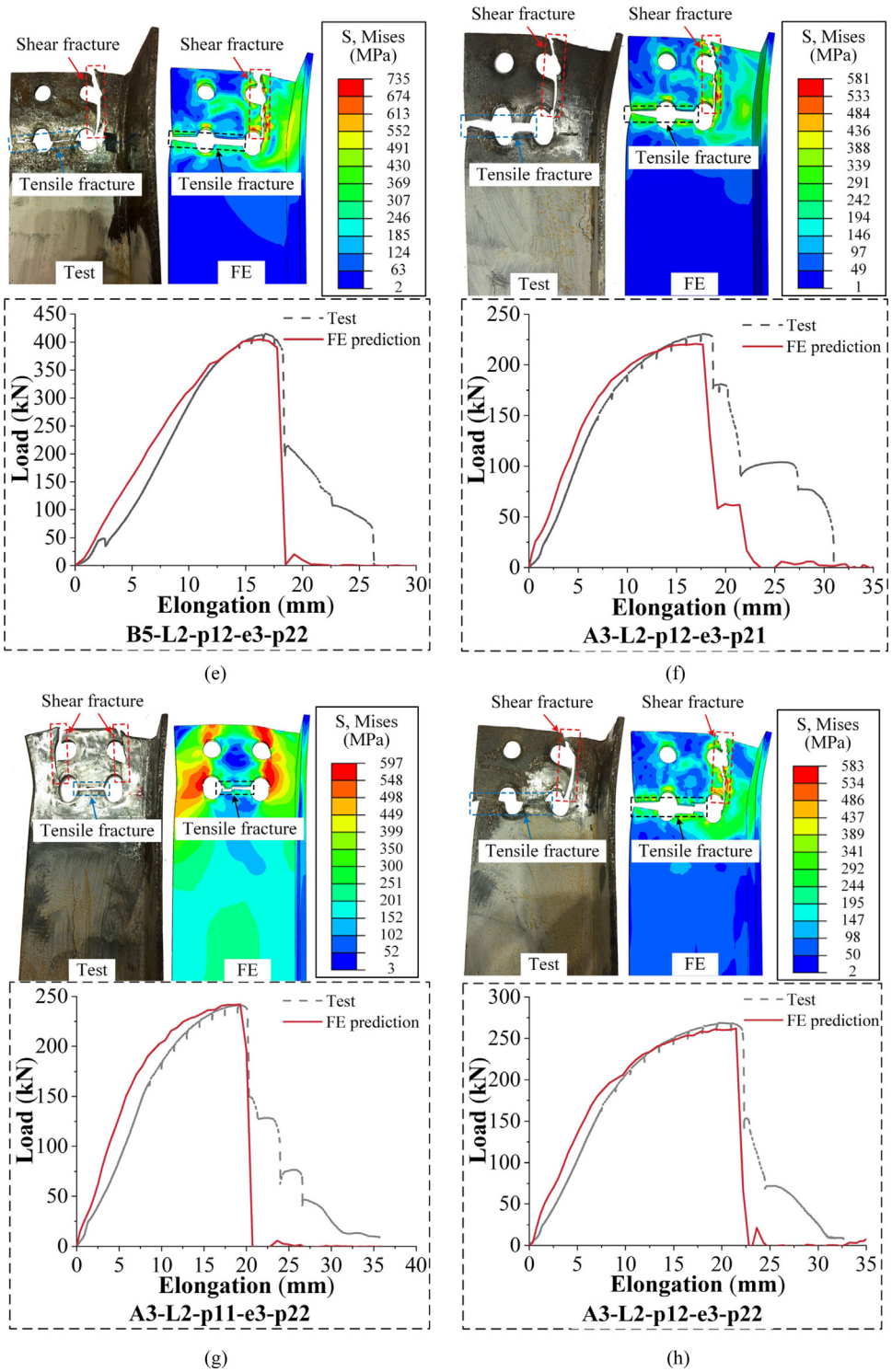

Fig. 10. (*continued*).

strength. Similar findings were obtained by focusing on the parameter of the transverse pitch. According to Table 4, it can be confirmed that the deformation capacity of the tensile angles was also enhanced with increasing transverse pitch and edge distance.

The influence of the block shear strength of the S690 steel angles with varied unconnected leg lengths is shown in Fig. 7 and listed in Table 4. As mentioned above, the connected leg length was constant, and only the unconnected leg length was varied (i.e., from 65 to 85 mm). After increasing the unconnected leg length from 65 to 85 mm, the ultimate load of the tension angles was not significantly affected, whereas the deformation capacity of the S690 steel angle was weakened.

5. Finite element analyses

5.1. Modelling strategies

To further study the block shear behaviour of the bolted tension angles, numerical models were established using ABAQUS software. The modelling approach adopted in this study was identical to that

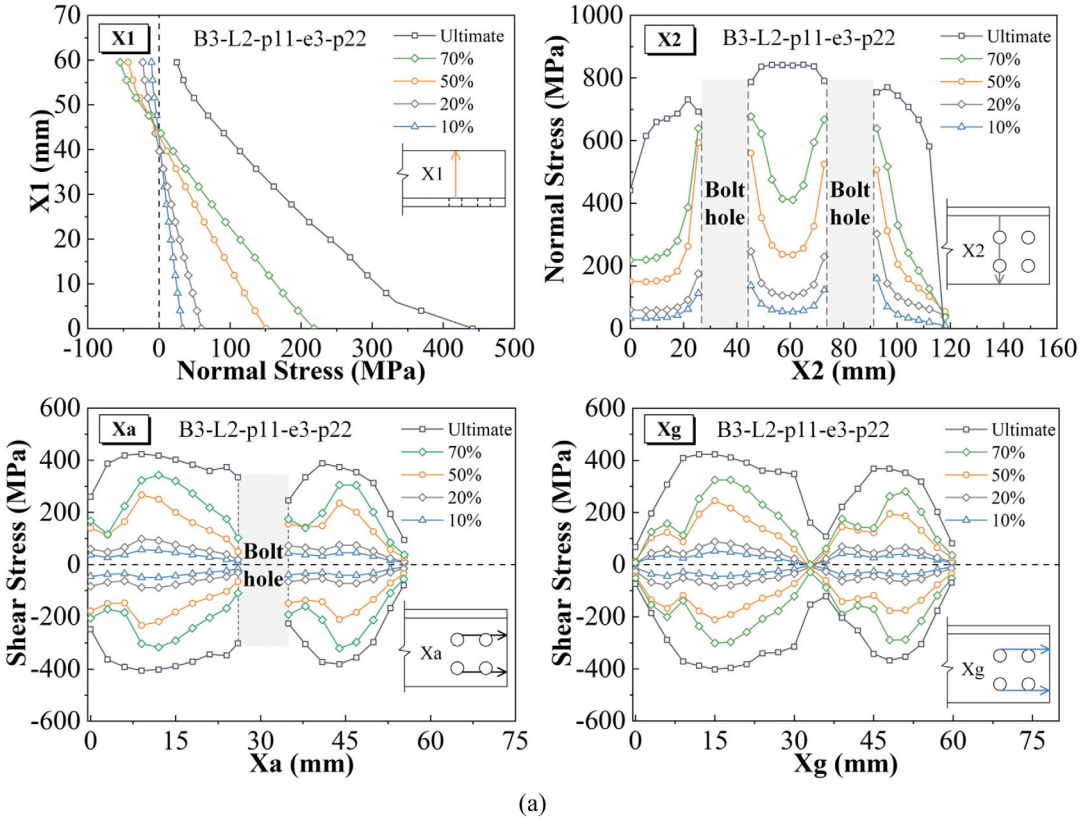

(a)

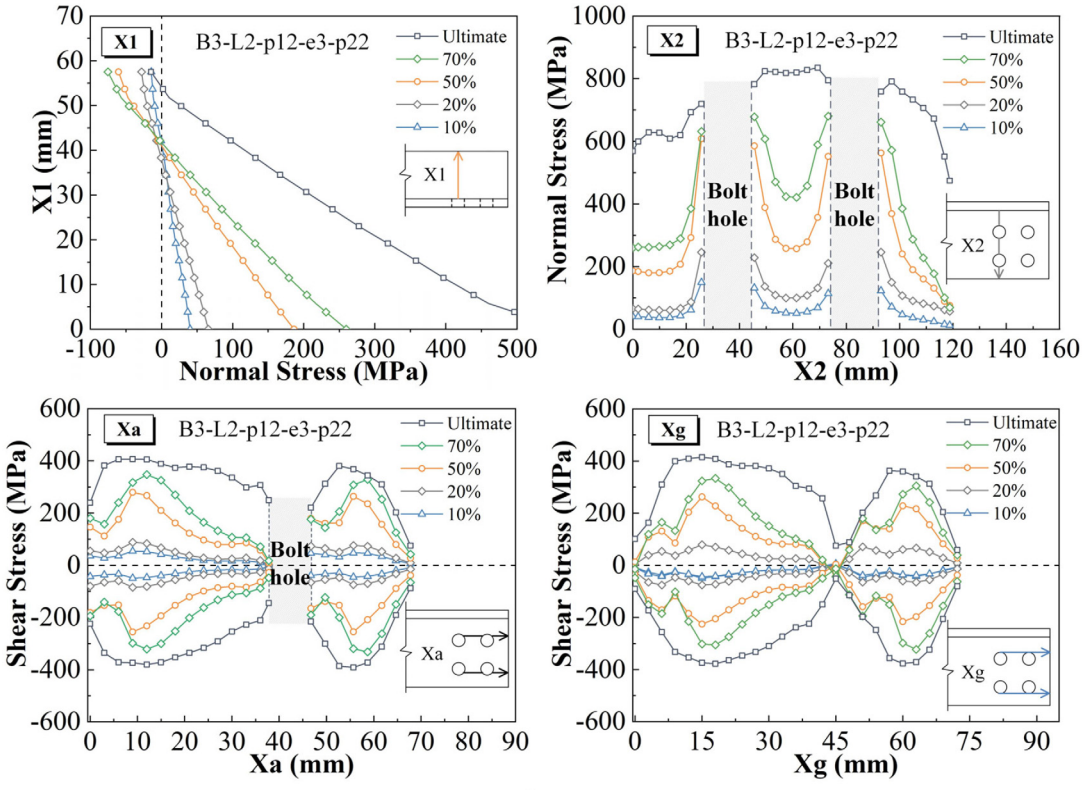

(b)

Fig. 11. Damage evolution of the FE models: (a) B3-L2-p11-e3-p22, (b) B3-L2-p12-e3-p22, (c) A3-L2-p11-e3-p22 and (d) A3-L2-p12-e3-p22.

described in [44], including the element formulation, material model, contact property, and boundary constraints. In particular, C3D8R elements considering hourglass control were adopted to develop the test specimens. To reproduce the interactive behaviour among the contacting surfaces of elements, hard contact in the normal direction along with penalty friction in the tangent direction was used. To simulate the end constraints, kinematic coupling was utilised to restrain the

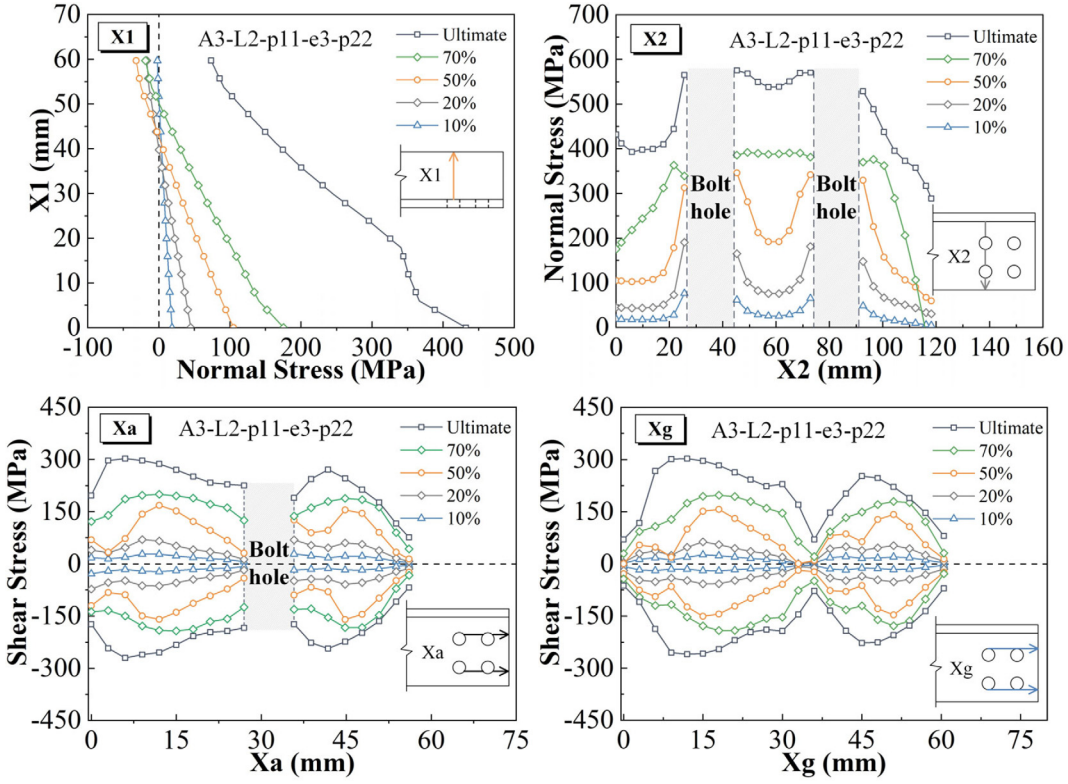

(c)

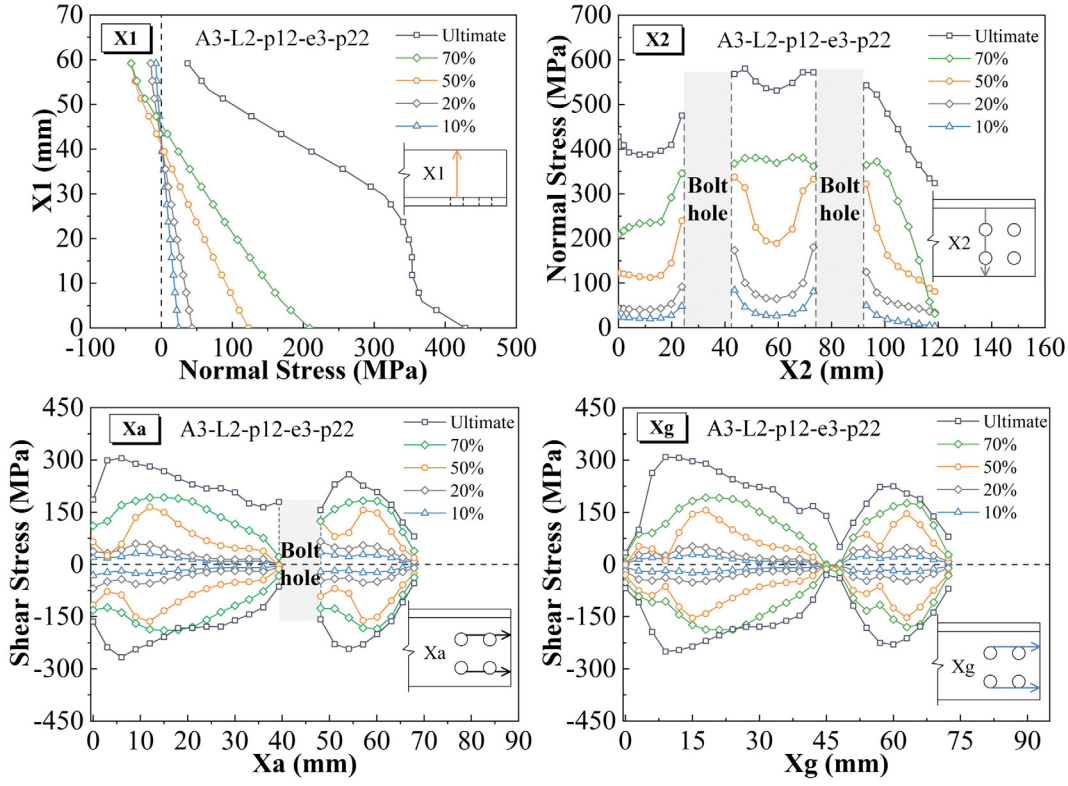

(d)

Fig. 11. (*continued*).

gusset plates, but the translational movement of the gusset plates in the longitudinal direction of the angle (U3 in Fig. 9) was released. Elastic spring elements were arranged at the gusset plate ends to reproduce the elastic deformation of the test rig. The spring stiffness was calibrated according to the initial slope of the load–elongation curves. An explicit solver was adopted to replicate the loading procedure with displacement applied to the end of the gusset plate.

In the inelastic material model, the von Mises yield criterion with isotropic hardening was adopted. The true stress–true strain (σ–ε) curves were input as material parameters [47]. Prior to necking, σ and ε were calculated as follows: $\sigma = \sigma_{eng}$ (1+ ε_{eng}) and ε = ln (1+ ε_{eng}). After necking, the σ–ε curve was assumed to be linear, and an iterative process was utilised to match the test response. The "Damage for Ductile Metals" model [47] was adopted to simulate the steel fracture. Cracking and strength decline of the steel was quantified by the fracture strain index and damage evolution index in the material model, and the Johnson–Cook damage model [48] was applied using a trial-and-error procedure. It is worth noting that the Johnson–Cook model is governed by stress triaxiality, and hence the parameter of shear (e.g., the Lode angle) was not considered. However, the focus of this study was the block shear strength dominated by cracking of the tension plane, which may be appreciably affected by the stress triaxiality. Therefore, we conclude that the implementation of the Johnson–Cook model in the current study was viable from the perspective of the strength of the specimens. The feasibility and limitations of adopting an iterative method for quantifying cracking in numerical analyses are discussed in the literature [49–53]. Fig. 9 presents a typical numerical model of the test specimens.

5.2. Analysis results and discussion

Based on the numerical modelling strategy, the ratio of the tensile strength of the test specimens (P_{test}) to the numerical prediction (P_{FE}) was extracted and the details are listed in Table 2. For S690 HSS angles, the P_{test}/P_{FE} ranged from 0.97 to 1.02, with an average of 0.99 and a coefficient of variation (CoV) of 0.018. Comparatively, a P_{test}/P_{FE} range of 0.91–1.01 was obtained for S275 angles, with an average of 0.98 and a CoV of 0.034.

The FE response curves and predicted failure patterns of the representative specimens were extracted and are shown in Fig. 10. The test responses up to the cracking of the tensile plane were accurately captured by the FE models. For S690 HSS and S275 NSS specimens governed by the BS1 mode, the failure was caused by necking and cracking of the net tension plane, and the inception of cracking of the shear plane followed. For most specimens exhibiting the BS2 mode except for B3-L2-p12-e3-p21, the block shear failure was commenced by necking of the connected leg toe.

To offer a comprehensive understanding of the block shear behaviour of the test specimens, the stress distributions (i.e., normal stress distribution over the critical section and shear stress over the various shear planes) of specimens B3-L2-p11-e3-p22 and A3-L2-p11-e3-p22 failing by the BS1 mode and comparison group B3-L2-p12-e3-p22 and A3-L2-p12-e3-p22 failing by the BS2 mode were collected. For normal stress, the tensile stress is positive. For the shear stress, the positive and negative values represent the shear stress at the shear planes close to the unconnected leg and that close to the connected leg toe, respectively. To capture the stress evolution at critical planes, the normal stress and shear stress at different loading stages (i.e., 10%, 20%, 50%, 70%, and 100% of P_{FE}) in the numerical models were extracted, as shown in Fig. 11.

According to the normal stress evolution at the critical section (Fig. 11), uneven normal stress at the tension plane (path X2) was evident at the initial loading level for all specimens, and the peak stress was captured close to the edge of the bolt hole because of the stress concentration. Stress redistribution was triggered in the later stage, where the angle sections developed inelasticity. Upon reaching the ultimate state, the uneven tensile stress near the bolt hole over the tension plane was less pronounced for both S690 HSS and S275 NSS angles failing by the two block shear modes. Furthermore, the net tension plane for S690 HSS and S275 NSS angles achieved tensile stress beyond the yield strength of the material at the ultimate load. This finding was in line with the measured strain distribution trends mentioned above and those discussed in the literature. It is also important to note that, for specimens governed by the BS1 mode, unloading at path X2 (close to the toe of the connected leg) was more evident compared with those failing by the BS2 mode at the ultimate load. Comparatively, for the unconnected leg, the normal stress distribution pattern was linear at the initial loading stage (path X1), and the toe was in compression. With a further increase in the loading, the compression at the unconnected leg toe was alleviated and reversed to tension at the ultimate load for most models, which is in line with the measured strain distributions discussed above. The normal stress distributions of S690 HSS and S275 angles over the unconnected leg were similar during the early loading stages, whereas the difference became evident during the ultimate stage. For both S690 HSS and S275 NSS angles, the shear stress evolution over the active shear plane (path Xa) and the shear stress evolution over the gross shear plane (path Xg) confirmed the material's ability to mobilise shear strength, and the nonuniformity of the shear stress at these two planes was mitigated with an increasing load. When the ultimate strength was reached, a comparison between the shear stress over the active shear plane and the gross shear plane showed that inelasticity was well developed at the former, confirming that the effectiveness of using the active shear plane for quantifying shear failure. These observations reaffirm the findings of Teh et al. [37,38].

It is also important to note that the tensile stress distribution mode of the critical section varied for specimens governed by different failure modes. For specimens failing by the BS1 mode, the maximum tensile stress at the net tension plane was concentrated at the region between two bolt holes, whereas the tensile stress outside the shear block was relatively lower. Comparatively, for specimens failing by the BS2 mode with a larger aspect ratio of the shear block, the tensile stress at the toe of the connected leg was also significant.

5.3. Additional parametric studies

To confirm the influence of the affected parameters on the block shear behaviour of double-line bolted tension angles, additional parametric numerical investigations were conducted. The main parameters included the end distance, edge distance, connected leg length, and unconnected leg length, which were not fully examined in the test programme. In addition, the equal angle section which had not been investigated in the test was studied through the FE analysis (e.g. No. 8 model B-Bt2-e1-S125T125-Ed24). For consistency, the parallel pitch and transverse pitch were set as 47.7 and 47.4 mm, respectively, for all FE models. The numerical models were represented by model labels. The label for each model starts with B, representing S690 steel. The value Bt represents the number of bolt rows. e1, e2, and e3 represent the edge distances of 22, 27, and 36 mm, respectively. S and T indicate the connected and unconnected leg lengths of the steel angle, respectively. Ed is the end distance of the model. Consider model B-Bt3-e1-S125T65-Ed24 as an example: B represents S690 steel and Bt3 means that the bolt row number is three. e1 means that the edge distance is 22 mm. S125T65 indicates that the connected and unconnected leg lengths of the angle are 125 and 65 mm, respectively. Ed24 means that the end distance is 24 mm.

Table 6 and Fig. 12 summarise the analysis results of the designed models. The analysis results confirmed that all FE models were dominated by the BS2 mode. It was confirmed that increasing the end distance increases the S690 steel angles' block shear strength by increasing the length of the shear plane. As expected, an increase in the edge distance leads to an increase in the S690 steel angles' block shear strength owing to the higher resistance of the tension plane. In addition,

Table 5
Comparisons between predictions of design equations and the test results.

Specimen	Considering failure mode BS1							Considering failure mode BS2							Min value of failure mode BS1 and BS2						
	$\frac{P_{test}}{P_{AISC}}$	$\frac{P_{test}}{P_{EC3}}$	$\frac{P_{test}}{P_{CSA}}$	$\frac{P_{test}}{P_{T\&Y}}$	$\frac{P_{test}}{P_{Topkaya}}$	$\frac{P_{test}}{P_{T\&D}}$	$\frac{P_{test}}{P_{AIJ}}$	$\frac{P_{test}}{P_{AISC}}$	$\frac{P_{test}}{P_{EC3}}$	$\frac{P_{test}}{P_{CSA}}$	$\frac{P_{test}}{P_{T\&Y}}$	$\frac{P_{test}}{P_{Topkaya}}$	$\frac{P_{test}}{P_{T\&D}}$	$\frac{P_{test}}{P_{AIJ}}$	$\frac{P_{test}}{P_{AISC}}$	$\frac{P_{test}}{P_{EC3}}$	$\frac{P_{test}}{P_{CSA}}$	$\frac{P_{test}}{P_{T\&Y}}$	$\frac{P_{test}}{P_{Topkaya}}$	$\frac{P_{test}}{P_{T\&D}}$	$\frac{P_{test}}{P_{AIJ}}$
B3-L2-p12-e1-p22	0.92	1.01	0.81	0.85	0.73	0.77	0.82	**1.09**	**1.16**	**1.19**	**1.07**	**0.94**	**0.98**	**1.02**	1.09	1.16	1.19	1.07	0.94	0.98	1.02
B3-L2-p12-e2-p22	1.00	1.11	0.90	0.94	0.81	0.85	0.91	**1.13**	**1.19**	**1.26**	**1.12**	**0.99**	**1.02**	**1.06**	1.13	1.19	1.26	1.12	0.99	1.02	1.06
B3-L2-p12-e3-p22	1.06	**1.17**	0.95	0.99	0.85	0.89	0.96	**1.08**	1.13	**1.25**	**1.08**	**0.96**	**0.99**	**1.02**	1.08	1.17	1.25	1.08	0.96	0.99	1.02
B3-L2-p12-e3-p21	1.07	**1.20**	0.90	0.99	0.84	0.89	0.96	**1.09**	1.15	**1.21**	**1.08**	**0.95**	**0.98**	**1.02**	1.09	1.20	1.21	1.08	0.95	0.98	1.02
B3-L2-p11-e3-p22[a]	**1.17**	**1.28**	1.00	1.06	0.88	0.96	0.99	1.08	1.12	**1.25**	**1.07**	**0.94**	**0.98**	**0.99**	1.17	1.28	1.25	1.07	0.94	0.98	0.99
B3-L3-p12-e3-p22	0.93	1.04	0.77	0.85	0.72	0.76	0.82	**1.10**	**1.17**	**1.15**	**1.07**	**0.94**	**0.97**	**1.02**	1.10	1.17	1.15	1.07	0.94	0.97	1.02
B3-L3-p12-e3-p21	0.92	1.05	0.72	0.83	0.69	0.74	0.80	**1.11**	**1.19**	**1.10**	**1.07**	**0.92**	**0.96**	**1.02**	1.11	1.19	1.10	1.07	0.92	0.96	1.02
B3-L3-p11-e3-p22	1.11	1.22	0.85	0.96	0.78	0.86	0.89	**1.17**	**1.23**	**1.20**	**1.12**	**0.95**	**1.01**	**1.03**	1.17	1.23	1.20	1.12	0.95	1.01	1.03
B5-L2-p12-e1-p22	0.90	0.99	0.81	0.84	0.72	0.76	0.81	**1.09**	**1.15**	**1.19**	**1.07**	**0.95**	**0.98**	**1.02**	1.09	1.15	1.19	1.07	0.95	0.98	1.02
B5-L2-p12-e3-p22	1.07	**1.18**	0.96	1.01	0.86	0.90	0.97	**1.09**	1.14	**1.26**	**1.09**	**0.97**	**1.00**	**1.03**	1.09	1.18	1.26	1.09	0.97	1.00	1.03
Mean	1.02	1.13	0.87	0.93	0.79	0.84	0.89	1.10	1.16	1.21	1.08	0.95	0.99	1.02	**1.11**	**1.20**	**1.20**	**1.09**	**0.95**	**0.99**	**1.02**
CoV	0.088	0.083	0.099	0.084	0.083	0.085	0.077	0.023	0.026	0.042	0.016	0.018	0.017	0.016	0.029	0.035	0.043	0.017	0.019	0.018	0.016
A3-L2-p12-e1-p22	0.94	1.23	0.89	1.07	0.80	0.79	1.03	**1.12**	**1.30**	**1.28**	**1.24**	**1.02**	**1.01**	**1.18**	1.12	1.30	1.28	1.24	1.02	1.01	1.18
A3-L2-p12-e3-p22	1.12	**1.47**	1.06	**1.28**	0.96	0.95	**1.23**	**1.12**	1.27	**1.36**	1.25	**1.04**	**1.03**	1.17	1.12	1.47	1.36	1.28	1.04	1.03	1.23
A3-L2-p12-e3-p21	1.11	**1.52**	0.98	**1.27**	0.92	0.91	**1.23**	**1.11**	1.28	**1.28**	1.24	**1.01**	**1.00**	1.16	1.11	1.52	1.28	1.27	1.01	1.00	1.23
A3-L2-p11-e3-p22[a]	**1.21**	**1.53**	1.09	**1.31**	0.97	0.99	**1.22**	1.11	1.22	**1.33**	1.20	**0.99**	**1.00**	1.11	1.21	1.53	1.33	1.31	0.99	1.00	1.22
A3-L3-p12-e3-p21	0.84	1.21	0.70	0.97	0.68	0.68	0.94	**1.01**	**1.22**	**1.05**	**1.13**	**0.88**	**0.88**	**1.07**	1.01	1.22	1.05	1.13	0.88	0.88	1.07
A3-L3-p11-e3-p22	1.17	**1.54**	0.94	1.24	0.87	0.90	1.14	**1.21**	1.38	**1.30**	**1.29**	**1.03**	**1.05**	**1.19**	1.21	1.54	1.30	1.29	1.03	1.05	1.19
Mean	1.07	1.41	0.94	1.19	0.87	0.87	1.13	1.11	1.28	1.27	1.23	0.99	0.99	1.15	**1.13**	**1.35**	**1.25**	**1.24**	**0.99**	**0.99**	**1.17**
CoV	0.122	0.100	0.136	0.106	0.115	0.120	0.099	0.053	0.041	0.080	0.042	0.052	0.056	0.038	0.061	0.094	0.085	0.058	0.057	0.061	0.050

[a]*Notes*: Specimens B3-L2-p11-e3-p22 and A3-L2-p11-e3-p22 failed by "BS1" mode. The design prediction missing the failure mode is underlined.

an increasing unconnected leg length, which appreciably affects the out-of-plane eccentricity, does not evidently influence the S690 steel angles' block shear strength. The variation in the connected leg length, which influences the in-plane eccentricity of the S690 angles, also has no obvious effect on the S690 steel angles' block shear strength. Note that the effect of load eccentricity on structural behaviour may be different in other scenarios, as observed in a recent study [54].

6. Design considerations

The accuracy of the design equations described in Section 2 for estimating the block shear strength of the test specimens was assessed. The material properties (Table 3) and measured dimensions (Table 2) were used in these equations. Note that the block shear strength of angles governed by BS1 and BS2 failure modes had been considered, and the lower of the two was taken as the design prediction. The design predictions were compared with the block shear strength obtained from the test, and the test-to-predicted ratios are listed in Table 5. It is noted that the Mean and CoV value of the test-to-predicted ratios were calculated without considering the specimens with missing failure mode. For the failure modes, the prediction by AISC [39] matched all the test results, whereas Eurocode 3 [40] had the lowest prediction accuracy, as the failure modes of six specimens were not captured. The other design methods in CSA [41] and AIJ [42] and approaches developed by Teh and Yazici [38], Topkaya [13], and Teh and Deierlein [43] may also lead to inconsistent predictions regarding the failure modes, and they were unable to fully capture the failure modes of the steel tension angles, as indicated in Table 5. These observations are understandable because of the underlying assumptions of the design equations may not apply to double-line bolted S690 steel tension angles failing by block shear. The net shear plane yielding assumption was adopted by Eurocode 3 [40] to calculate the shear plane resistance; hence, the shear resistance might be underestimated. In this context, for specimens governed by BS2 failure, the block shear capacity based on the BS1 mode by Eurocode 3 [40] was relatively lower, leading to inconsistent failure mode predictions. In contrast, the tensile resistance by design equations in CSA [41] was conservatively considered, and hence the block shear strength determined by the BS2 mode with a large tension plane was lower in several cases. Consequently, the failure patterns of the two specimens failing by the BS1 mode (i.e., B3-L2-p11-e3-p22 and A3-L2-p11-e3-p22) were missed. Similarly, the Topkaya's method [13] was prone to overestimate the shear resistance by considering an equivalent shear yield stress and the gross shear plane, and hence the BS1 mode was missed. Similar findings characterised the prediction equations by Teh and Deierlein [43]. In their method, the active shear plane fracture assumption was adopted. In this context, the block shear strength of specimens B3-L2-p11-e3-p22 and A3-L2-p11-e3-p22 considering the BS2 mode was lower than that in the BS1 mode; hence, the failure modes of the two specimens were not captured. For the prediction equation in AIJ, it was found that the failure modes of several NSS angles failing by the BS2 mode (i.e., Table 5) were missed. This could be because the shear resistance in AIJ [42] was conservatively considered; hence, post-yielding strain hardening of the shear plane was not fully exploited in the design equation. As a result, the block shear strength of these NSS specimens was governed by the BS1 mode using the design equations. It is interesting to note that AIJ [42] did not produce any inconsistent predictions for failure modes of S690 HSS specimens, owing to the fact that the post-yielding strain hardening of the material was insignificant. Teh and Yazici's equation [38] also excluded post-yielding strain hardening of the active shear plane, and hence the BS1 mode dominated the design for several NSS specimens (i.e., Table 5). However, Teh and Yazici's equation also did not capture the S690 steel angle failing by the BS1 mode, and the computed block shear strength based on the BS2 mode was lower.

As indicated in Table 5, the block shear strength predicted by Eurocode 3 [40] was overly conservative for both the S690 and S275 steel specimens. This was because the contribution of the shear resistance determined based on the net shear plane yielding (Table 1) was underestimated. Based on recent studies in the literature [37,38,43], there was sufficient test evidence supporting that the shear failure plane should be determined based on the active shear plane (Table 1) and the use of the net shear plane was conservative. Moreover, Eurocode 3 [40] did not consider the contribution of strain hardening at the shear failure plane, which may produce more conservative predictions for the S275 steel specimens with an evident strain hardening effect (Table 5). Although the strain hardening effect was considered by AISC [39], the selection of the net shear plane resulted in an underestimation of the shear resistance. Hence, conservative estimations of block shear strength were obtained. The safe predictions by CSA [41] were produced by conservative consideration of the uneven stress distribution on the tensile plane. Although AIJ [42] provided conservative predictions for S275 steel specimens because it did not consider the

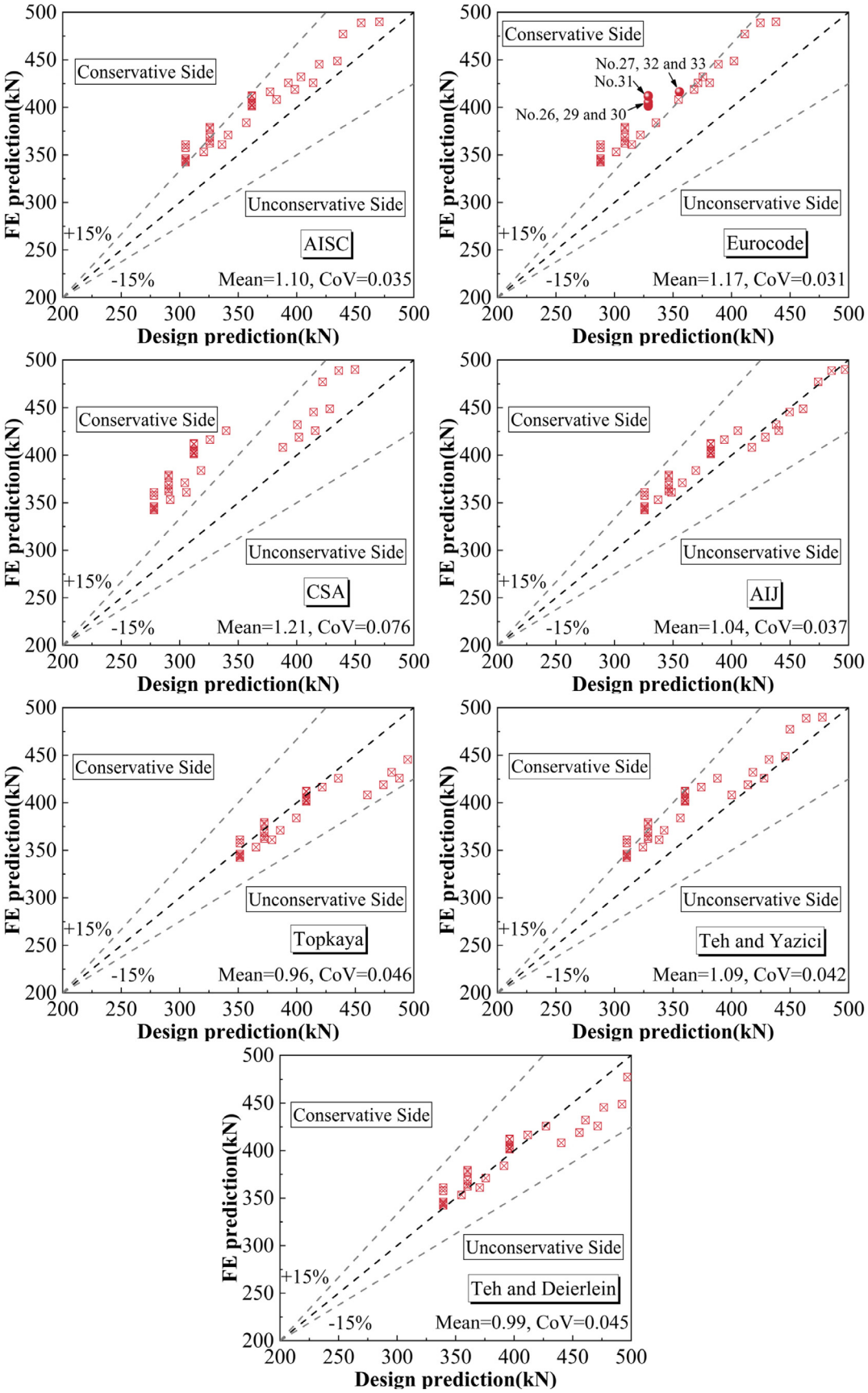

Fig. 12. Design predictions against FE results.

Table 6
Comparisons between predictions of design equations and numerical simulations.

No.	Models	Capacity (kN)	$\frac{P_{FE}}{P_{AISC}}$	$\frac{P_{FE}}{P_{EC3}}$	$\frac{P_{FE}}{P_{CSA}}$	$\frac{P_{FE}}{P_{T\&Y}}$	$\frac{P_{FE}}{P_{Topkaya}}$	$\frac{P_{FE}}{P_{T\&D}}$	$\frac{P_{FE}}{P_{AIJ}}$
1	B-Bt3-e1-S125T65-Ed24	408.16	1.07	1.15	1.05	1.02	0.89	0.93	0.98
2	B-Bt3-e1-S125T65-Ed30	418.94	1.05	1.14	1.04	1.01	0.88	0.92	0.98
3	B-Bt3-e1-S125T65-Ed36	425.85	1.03	1.12	1.02	1.00	0.87	0.90	0.97
4	B-Bt2-e1-S125T65-Ed24	343.45	1.13	1.19	1.24	1.11	0.98	1.01	1.05
5	B-Bt2-e1-S125T65-Ed30	353.24	1.10	1.17	1.21	1.09	0.97	0.99	1.05
6	B-Bt2-e1-S125T65-Ed36	361.10	1.07	1.15	1.18	1.07	0.95	0.97	1.04
7	B-Bt2-e1-S125T85-Ed24	342.24	1.12	1.19	1.23	1.10	0.97	1.01	1.05
8	B-Bt2-e1-S125T125-Ed24	346.07	1.13	1.20	1.24	1.11	0.98	1.02	1.06
9	B-Bt2-e1-S125T150-Ed24	344.97	1.13	1.20	1.24	1.11	0.98	1.02	1.06
10	B-Bt2-e1-S150T65-Ed24	357.71	1.17	1.24	1.29	1.15	1.02	1.05	1.10
11	B-Bt2-e1-S180T65-Ed24	360.97	1.18	1.25	1.30	1.16	1.03	1.06	1.11
12	B-Bt3-e2-S125T65-Ed24	431.98	1.07	1.15	1.08	1.03	0.90	0.94	0.99
13	B-Bt3-e2-S125T65-Ed30	445.28	1.06	1.15	1.07	1.03	0.90	0.93	0.99
14	B-Bt3-e2-S125T65-Ed36	448.75	1.03	1.12	1.05	1.01	0.88	0.91	0.97
15	B-Bt2-e2-S125T65-Ed24	362.23	1.11	1.17	1.25	1.10	0.97	1.01	1.05
16	B-Bt2-e2-S125T65-Ed30	371.00	1.09	1.15	1.22	1.08	0.96	0.99	1.04
17	B-Bt2-e2-S125T65-Ed36	383.92	1.08	1.14	1.21	1.08	0.96	0.98	1.04
18	B-Bt2-e2-S125T85-Ed24	364.62	1.12	1.18	1.25	1.11	0.98	1.01	1.05
19	B-Bt2-e2-S125T125-Ed24	368.72	1.13	1.19	1.27	1.12	0.99	1.02	1.06
20	B-Bt2-e2-S125T150-Ed24	368.58	1.13	1.19	1.27	1.12	0.99	1.02	1.06
21	B-Bt2-e2-S150T65-Ed24	377.75	1.16	1.22	1.30	1.15	1.01	1.05	1.09
22	B-Bt2-e2-S180T65-Ed24	379.18	1.16	1.23	1.31	1.15	1.02	1.05	1.09
23	B-Bt3-e3-S125T65-Ed24	477.15	1.09	1.16	1.13	1.06	0.92	0.96	1.01
24	B-Bt3-e3-S125T65-Ed30	488.69	1.07	1.15	1.12	1.05	0.92	0.95	1.01
25	B-Bt3-e3-S125T65-Ed36	489.90	1.04	1.12	1.09	1.03	0.90	0.93	0.99
26	B-Bt2-e3-S125T65-Ed24	401.43	1.11	1.22	1.29	1.11	0.98	1.01	1.05
27	B-Bt2-e3-S125T65-Ed30	416.36	1.10	1.17	1.28	1.11	0.99	1.01	1.06
28	B-Bt2-e3-S125T65-Ed36	425.78	1.08	1.15	1.25	1.10	0.98	1.00	1.05
29	B-Bt2-e3-S125T85-Ed24	402.75	1.11	1.22	1.29	1.12	0.99	1.02	1.05
30	B-Bt2-e3-S125T125-Ed24	402.37	1.11	1.22	1.29	1.12	0.99	1.02	1.05
31	B-Bt2-e3-S125T150-Ed24	405.46	1.12	1.23	1.30	1.13	0.99	1.02	1.06
32	B-Bt2-e3-S150T65-Ed24	412.24	1.14	1.25	1.32	1.14	1.01	1.04	1.08
33	B-Bt2-e3-S180T65-Ed24	411.59	1.14	1.25	1.32	1.14	1.01	1.04	1.08
		Mean	1.10	1.17	1.21	1.09	0.96	0.99	1.04
		CoV	0.035	0.031	0.076	0.042	0.046	0.045	0.037

Notes: The design prediction missing the failure mode is underlined.

strain hardening effect at the shear plane, it matched the test load of S690 specimens well. In particular, the average test-predicted ratios for S690 and S275 steel angle specimens based on AIJ [42] were 1.02 and 1.17 with CoV values of 0.016 and 0.050, respectively. Similarly, the conservative trend of the method by Teh and Yazici [38] also resulted from the fact that the strain hardening effect at the shear plane was excluded. From the statistical and strength perspective, the design equation proposed by Teh and Deierlein [43] gave slightly nonconservative predictions for both S690 and S275 specimens by considering full strain hardening at the active shear plane. Furthermore, nonconservative predictions were produced by the method proposed by Topkaya [13], because the gross shear plane was selected when computing the block shear strength, which overestimated the shear resistance. Accordingly, based on the limited experimental data, the AIJ [42] design equation provided reasonable predictions of the block shear strength and failure mode for S690 HSS angle specimens. It is noteworthy that the average test-predicted ratios of the S690 specimens were relatively lower than those of the S275 specimens. However, for steel angles with single-line bolted connections [44], the average test-predicted ratios of the S690 and S275 specimens were at the same level. This is because the tension planes in the double-line bolted angles were relatively larger than those of the single-line bolted angles. For the single-line bolted angles [44], the tensile loads were mainly resisted by the shear resistance of the shear plane. However, under a shear load, the advantage of NSS in ductility was not as significant as that of HSS; therefore, the test-predicted ratios of single-line bolted angles were similar. For the double-line bolted angles, the tensile resistance provided by the tension planes was more significant, which was beneficial to the development of the ductility of the NSS material. Therefore, the test-predicted ratios of the NSS specimens were higher than those of the HSS specimens.

The design methods were applied to the numerical results to further examine their effectiveness in assessing the block shear strength of steel angles. As demonstrated in Fig. 12, the design predictions were plotted against the FE results. These results match the findings obtained from the test data pool. In summary, all design methods, except Eurocode 3 [40], provided accurate predictions regarding the failure modes of numerical models. Eurocode 3 [40] did not capture failure modes of several models (marked in Fig. 12 using different labels and corresponding numbers) dominated by the BS2 mode. In terms of the accuracy in predicting the block shear strength of S690 models, AISC [39], Eurocode 3 [40], CSA [41], and Teh and Yazici [38] generally produced conservative predictions. In contrast, slightly nonconservative predictions were made by Teh and Deierlein [43]. Topkaya [13] provided evidently nonconservative predictions for FE models, in concurrence with the findings mentioned above. AIJ [42] produced reasonable predictions that are consistent with the test results. In particular, the average P_{FE}/P_{AIJ} was 1.04 and the CoV was 0.037.

7. Conclusions

The present experimental programme was aimed at studying the block shear behaviour of S690 HSS tension angles with a double-line bolted connection. Ten S690 specimens and six S275 NSS specimens were tested. The influences of the steel grade, connection configuration, and angle sections on the block shear behaviour of the bolted angles were thoroughly examined. Based on the experimental and numerical results, the accuracy and adequacy of design specifications in the United States, Europe, Canada, and Japan and prediction equations documented in the literature were examined. The following conclusions can be made from this study:

- The angles with the double-line bolted connection had two failure modes, depending on the connection configuration. For specimens with a relatively smaller shear plane area and a larger tension plane, the block shear failure mode with two shear failure planes was recorded. For the remaining specimens, block shear failure was characterised by one shear failure forming at a plane close to the unconnected leg of the angle.
- The block shear behaviour of the S690 HSS specimens resembled that of the NSS specimens. Generally, the block shear strength of the S690 steel angles increased with increasing bolt rows and parallel pitch. Comparably, an increasing transverse pitch and edge distance also contributed to the enhanced block shear strength because the tension plane area was increased. However, the length of the unconnected leg had no significant influence on the block shear strength. The influence of the essential factors on the block shear strength of S690 steel angles was further confirmed by an extensive parametric study covering a wider parameter spectrum.
- Based on the correlation among the test data pool, numerical results, and design equation predictions, it can be confirmed that Eurocode 3 [40], CSA [41], and design methods in the literature may produce inconsistent predictions for the failure modes of both S690 and S275 specimens and models. In contrast, the failure modes of the S690 specimens and models predicted by AIJ [42] were accurate. AISC [39] was able to capture the failure modes of all test specimens and numerical models. From the perspective of the accuracy of strength, it was found that Eurocode 3 [40], CSA [41], AIJ [42], AISC [39], and Teh and Yazici [38] generally provided conservative predictions of block shear strengths for both the S690 and S275 specimens. In comparison, AIJ [42] provided more reasonable predictions of the block shear strength for S690 specimens. Teh and Deierlein [43] provided slightly nonconservative predictions for both the S690 and S275 specimens, and more conservative predictions were made by Topkaya. Based on the limited experimental and numerical results, it is preliminarily recommended that the AISC design equations may be used to quantify the block shear resistance of double-line bolted S690 steel angles owing to the reasonable accuracy of the prediction results. Extended parametric analysis is currently underway, which may be used to give a full-fledged design method for the block shear resistance of double-line bolted S690 steel tension angles.

It is worth noting that the results obtained from this study were based on 6 mm thick steel angles, and the conclusions may not be extrapolated to cold-reduced steel with reduced thickness, because the ductility of the thin cold-reduced steel sheets would be lower than the hot-rolled steel plates used in this study [46].

CRediT authorship contribution statement

Ke Ke: Conceptualization, Methodology, Writing – reviewing & editing, Supervision, Funding acquisition, Project administration. **Mingyuan Zhang:** Formal analysis, Investigation, Data curation, Visualization . **Michael C.H. Yam:** Methodology, Writing – reviewing & editing, Resources. **Angus C.C. Lam:** Resources. **Junjie Wang:** Visualization, Writing – original draft. **Binghui Jiang:** Resources.

Declaration of competing interest

The authors declare that they have no known competing financial interests or personal relationships that could have appeared to influence the work reported in this paper.

Acknowledgments

This work was supported by the Research Grants Council of the Hong Kong Special Administrative Region, China (Grant No. PolyU 152650/16E). The National Natural Science Foundation of China provided partial funding support (Grant Nos. 51890902 and 51708197). The first author would also like to extend sincere appreciation to his wife Siqin, his 15-month-old daughter Yutong, and all families for their constant support and understanding, particularly during this challenging period.

References

[1] J.G. Orbison, M.E. Wagner, W.P. Fritz, Tension plane behavior in single-row bolted connections subject to block shear, J. Constr. Steel Res. 49 (3) (1999) 225–239.
[2] C. Topkaya, Finite element modeling of block shear failure in coped steel beams, J. Constr. Steel Res. 63 (4) (2007) 544–553.
[3] M.C.H. Yam, Y.C. Zhong, A.C.C. Lam, V.P. Iu, An investigation of the block shear strength of coped beams with a welded clip angle connection—part I: experimental study, J. Constr. Steel Res. 63 (1) (2007) 96–115.
[4] C. Fang, A.C.C. Lam, M.C.H. Yam, K.S. Seak, Block shear strength of coped beams with single-sided bolted connection, J. Constr. Steel Res. 86 (2013) 153–166.
[5] A.C.C. Lam, C. Fang, M.C.H. Yam, W. Wang, V.P. Iu, Block shear strength and design of coped beams with double bolt-line connections, Eng. Struct. 100 (2015) 293–307.
[6] M.C.H. Yam, C. Fang, A.C.C. Lam, J.J.R. Cheng, Local failures of coped steel beams—a state-of-the-art review, J. Constr. Steel Res. 102 (2014) 217–232.
[7] J.M. Ricles, J.A. Yura, Strength of double-row bolted-web connections, J. Struct. Eng. 109 (1) (1983) 126–142.
[8] S.G. Hardash, R. Bjorhovde, New design criteria for gusset plates in tension, Eng. J. 22 (2) (1985) 77–94.
[9] M.K.S. Madugula, S. Mohan, Angles in eccentric tension, J. Struct. Eng. 114 (10) (1988) 2387–2396.
[10] H.I. Epstein, An experimental study of block shear failure of angles in tension, Eng. J. 29 (2) (1992) 75–84.
[11] T.J. Cunningham, J.G. Orbison, R.D. Ziemian, Assessment of American block shear load capacity predictions, J. Constr. Steel Res. 35 (3) (1995) 323–338.
[12] G.L. Kulak, G.Y. Grondin, Block shear failure in steel members–a review of design practice, Eng. J. 38 (4) (2001) 199–203.
[13] C. Topkaya, A finite element parametric study on block shear failure of steel tension members, J. Constr. Steel Res. 60 (11) (2004) 1615–1635.
[14] C. Topkaya, Block shear failure of gusset plates with welded connections, Eng. Struct. 29 (1) (2007) 11–20.
[15] P.L. Rosenstrauch, M. Sanayei, B.R. Brenner, Capacity analysis of gusset plate connections using the whitmore, block shear, global section shear, and finite element methods, Eng. Struct. 48 (2013) 543–557.
[16] M.J. Samimi, J.A. Marnani, S.M.S. Otaghsaraie, S.R.S. Otaghsaraie, Block shear experimental and numerical studies on hot rolled channel and gusset plate with staggered bolted connection, Thin-Walled Struct. 108 (2016) 153–162.
[17] Y.Z. Wang, G.Q. Li, Y.B. Wang, Y.F. Lyu, H. Li, Ductile fracture of high strength steel under multi-axial loading, Eng. Struct. 210 (2020) 110401.
[18] Y.B. Wang, G.Q. Li, W. Cui, S.W. Chen, F.F. Sun, Experimental investigation and modeling of cyclic behavior of high strength steel, J. Constr. Steel Res. 104 (2015) 37–48.
[19] Y.Z. Wang, A. Kanvinde, G.Q. Li, Y.B. Wang, A new constitutive model for high strength structural steels, J. Constr. Steel Res. 182 (2021) 106646.
[20] G. Shi, X. Zhu, H. Ban, Material properties and partial factors for resistance of high-strength steels in China, J. Constr. Steel Res. 121 (2016) 65–79.
[21] H.C. Ho, X. Liu, K.F. Chung, A.Y. Elghazouli, M. Xiao, Hysteretic behaviour of high strength S690 steel materials under low cycle high strain tests, Eng. Struct. 165 (2018) 222–236.
[22] A.D.C. Sousa, A. Nussbaumer, Multiaxial ultra low cycle fatigue in welded high strength steel structural components, J. Constr. Steel Res. 153 (2019) 473–482.
[23] K. Ke, Y.H. Xiong, M.C.H. Yam, A.C.C. Lam, K.F. Chung, Shear lag effect on ultimate tensile capacity of high strength steel angles, J. Constr. Steel Res. 145 (2018) 300–314.
[24] H. Fang, T.M. Chan, B. Young, Experimental and numerical investigations of octagonal high-strength steel tubular stub columns under combined compression and bending, J. Struct. Eng. 147 (1) (2021) 04020282.
[25] H. Fang, T.M. Chan, B. Young, Behaviour of octagonal high-strength steel tubular stub columns, J. Struct. Eng. 145 (12) (2019) 04019150.
[26] H. Fang, T.M. Chan, Buckling resistance of welded high-strength-steel box-section members under combined compression and bending, J. Constr. Steel Res. 162 (2019) 105711.
[27] H. Fang, T.M. Chan, Resistance of axially loaded hot-finished S460 and S690 steel square hollow stub columns at elevated temperatures, Structures 17 (2019) 66–72.

[28] H.T. Li, B. Young, Behaviour of cold-formed high strength steel RHS under localised bearing forces, Eng. Struct. 183 (2019) 1049–1058.
[29] H.T. Li, B. Young, Cold-formed high-strength steel tubular structural members under combined bending and bearing, J. Struct. Eng. 145 (8) (2019) 04019081.
[30] H.T. Li, B. Young, Cold-formed high strength steel SHS and RHS beams at elevated temperatures, J. Constr. Steel Res. 158 (2019) 475–485.
[31] K. Ke, M.C.H. Yam, H. Zhang, A.C. Lam, X. Zhou, High-strength steel frames with SMA connections in self-centring energy-dissipation bays: Insights and a multimodal nonlinear static procedure, Smart Mater. Struct. 29 (12) (2020) 125020.
[32] Y.Y. Chen, K. Ke, Seismic performance of high-strength-steel frame equipped with sacrificial beams of non-compact sections in energy dissipation bays, Thin-Walled Struct. 139 (2019) 169–185.
[33] K. Ke, M.C.H. Yam, L. Deng, Q.Y. Zhao, A modified DEB procedure for estimating seismic demands of multi-mode-sensitive damage-control HSSF-EDBs, J. Constr. Steel Res. 150 (2018) 329–345.
[34] X. Tian, M. Su, M. Lian, F. Wang, S. Li, Seismic behavior of K-shaped eccentrically braced frames with high-strength steel: shaking table testing and FEM analysis, J. Constr. Steel Res. 143 (2018) 250–263.
[35] F. Hu, G. Shi, Y. Shi, Experimental study on seismic behavior of high strength steel frames: global response, Eng. Struct. 131 (2017) 163–179.
[36] J.M. Gross, J.G. Orbison, R.D. Ziemian, Block shear tests in high-strength steel angles, Eng. J. 32 (3) (1995) 117–122.
[37] L.H. Teh, D.D.A. Clements, Block shear capacity of bolted connections in cold-reduced steel sheets, J. Struct. Eng. 138 (4) (2011) 459–467.
[38] L.H. Teh, V. Yazici, Unconventional block shear failures of bolted connections in cold-reduced steel sheets, Eng. Struct. 56 (2013) 567–571.
[39] American Institute of Steel Construction, Specification for Structural steel buildings, in ANSI/AISC360-16, 2016, Chicago, America.
[40] European Committee for Standardization, Design of steel structures, Part 1.8: Design of joints, in EN 1993-1-8, 2005, Brussels, Belgium.
[41] Canadian Standards Association, Design of Steel Structures, CSA S16–14, 2014.
[42] Architectural Institute of Japan (AIJ), Recommendation for Limit State Design of Steel Structures, Tokyo, Japan (in Japanese), 2002.
[43] L.H. Teh, G.G. Deierlein, Effective shear plane model for tearout and block shear failure of bolted connections, Eng. J. 54 (2017) 181–194.
[44] B. Jiang, M.C.H. Yam, K. Ke, A.C. Lam, Q. Zhao, Block shear failure of S275 and S690 steel angles with single-line bolted connections, J. Constr. Steel Res. 170 (2020) 106068.
[45] ASTM, A370, Standard Test Methods and Definitions for Mechanical Testing of Steel Products, American Society for Testing and Material, Philadelphia, PA, 2002.
[46] L.H. Teh, M.E. Uz, Block shear failure planes of bolted connections-direct experimental verifications, J. Constr. Steel Res. 111 (2015) 70–74.
[47] ABAQUS Analysis User's Manual, ABAQUS Standard, 2012, Version 6.12.
[48] G.R. Johnson, W.H. Cook, Fracture characteristics of three metals subjected to various strains, strain rates, temperatures and pressures, Eng. Fract. Mech. 21 (1985) 31–48.
[49] L.J. Jia, H. Kuwamura, Ductile fracture model for structural steel under cyclic large strain loading, J. Constr. Steel Res. 106 (2015) 110–121.
[50] F.F. Liao, W. Wang, Y.Y. Chen, Ductile fracture prediction for welded steel connections under monotonic loading based on micromechanical fracture criteria, Eng. Struct. 94 (2015) 16–28.
[51] L. Li, W. Wang, Y.Y. Chen, Y. Lu, Effect of beam web bolt arrangement on catenary behaviour of moment connections, J. Constr. Steel Res. 104 (2015) 22–36.
[52] F. Sadek, J.A. Main, H.S. Lew, Y.H. Bao, Testing and analysis of steel and concrete beam–column assemblies under a column removal scenario, J. Struct. Eng. 137 (9) (2011) 881–892.
[53] B. Yang, K.H. Tan, Numerical analyses of steel beam–column joints subjected to catenary action, J. Constr. Steel Res. 70 (70) (2012) 1–11.
[54] B. Shanmugasundaram, V. Natesan, M. Madhavan, Effect of staggered bolted connections on CFS channel sections, J. Constr. Steel Res. 173 (2020) 106215.